


# Biophysical *Journal*

Volume 116  
Number 1  
January 8, 2019

The Premier Journal of Quantitative Biology

[www.biophysj.org](http://www.biophysj.org)

 Biophysical Society

CellPress

# Highly Efficient Protein-free Membrane Fusion: A Giant Vesicle Study

Rafael B. Lira,<sup>1,2</sup> Tom Robinson,<sup>2</sup> Rumiana Dimova,<sup>2,\*</sup> and Karin A. Riske<sup>1,\*</sup>

<sup>1</sup>Departamento de Biofísica, Universidade Federal de São Paulo, São Paulo, Brazil and <sup>2</sup>Department of Theory and Bio-Systems, Max Planck Institute of Colloids and Interfaces, Potsdam, Germany

**ABSTRACT** Membrane fusion is a ubiquitous process in biology and is a prerequisite for many intracellular delivery protocols relying on the use of liposomes as drug carriers. Here, we investigate in detail the process of membrane fusion and the role of opposite charges in a protein-free lipid system based on cationic liposomes (LUVs, large unilamellar vesicles) and anionic giant unilamellar vesicles (GUVs) composed of different palmitoylcholine (POPC)/palmitoylphosphatidylglycerol (POPG) molar ratios. By using a set of optical-microscopy- and microfluidics-based methods, we show that liposomes strongly dock to GUVs of pure POPC or low POPG fraction (up to 10 mol%) in a process mainly associated with hemifusion and membrane tension increase, commonly leading to GUV rupture. On the other hand, docked LUVs quickly and very efficiently fuse with negative GUVs of POPG fractions at or above 20 mol%, resulting in dramatic GUV area increase in a charge-dependent manner; the vesicle area increase is deduced from GUV electrodeformation. Importantly, both hemifusion and full fusion are leakage-free. Fusion efficiency is quantified by the lipid transfer from liposomes to GUVs using fluorescence resonance energy transfer (FRET), which leads to consistent results when compared to fluorescence-lifetime-based FRET. We develop an approach to deduce the final composition of single GUVs after fusion based on the FRET efficiency. The results suggest that fusion is driven by membrane charge and appears to proceed up to charge neutralization of the acceptor GUV.

## INTRODUCTION

Membrane fusion is a ubiquitous process in biology, fundamental in events such as egg fertilization and viral infection as well as hormone and neurotransmitter release (1,2). Membrane fusion follows successive steps, including 1) docking of the opposing bilayers; 2) membrane adhesion and lipid destabilization; 3) fusion of the outer leaflets, termed hemifusion; 4) fusion pore formation and expansion of the fusion neck; and eventually 5) full fusion (1,3). In the docked state, the opposing membranes are in direct physical contact, but their bilayers are intact. The subsequent merging of the membranes' outer leaflets (hemifusion) results in mixing of lipids from both external monolayers, but the aqueous contents encapsulated by the membranes are still separated by a single bilayer. Eventually, a small fusion pore opens, and it may or may not expand (1–6). Full fusion is the result of complete pore expansion and merging of both aqueous compartments, yielding a final membrane with an area equal to the sum of the areas of the otherwise separated

membranes. In cells, membrane docking followed by lipid destabilization usually rely on a complex protein machinery, e.g., the SNARE proteins in synaptic vesicles and the viral fusion proteins in viral infection. Fusion can also be triggered by other (nonphysiological) stimuli.

Studying membrane fusion *in vivo* is challenging because of its fast, dynamic, and complex nature. For this reason, many *in vitro* systems have been developed in the last few years (see, e.g., (7)) to unravel the molecular requirements of fusion and, in some cases, its intermediates. In synthetic systems, a number of distinct fusogenic stimuli—such as reconstituted proteins (8,9), electric pulses (10,11), laser irradiation (12), plasmonic and nanoheaters (13,14), fusion peptides (15,16), and polymers (17,18)—can mediate fusion, and it is assumed that most fusion events transit through the same fusion intermediates (except in the case of fusion induced by electromagnetic fields), even though they may differ in dynamics. Methods for detecting fusion and its intermediates usually rely on quenching or dequenching of fluorescent lipids present in the membrane, yielding a change in signal (decrease or increase, respectively) upon fusion (see, e.g., (6,19–21)). Lipid mixing is required, but alone, it is insufficient to assess complete fusion. In fact, extensive lipid mixing in instances of outer

Submitted August 20, 2018, and accepted for publication November 19, 2018.

\*Correspondence: [dimova@mpikg.mpg.de](mailto:dimova@mpikg.mpg.de) or [kariske@unifesp.br](mailto:kariske@unifesp.br)

Editor: Tobias Baumgart.

<https://doi.org/10.1016/j.bpj.2018.11.3128>

© 2018 Biophysical Society.





leaflet merging (hemifusion) or merging of the outer and inner monolayers can occur without simultaneous mixing of the internal bulk contents, possibly because of the formation of a small fusion pore that does not expand (22). Importantly, *in vitro* fusion is classically studied in populations of small or large liposomes (SUVs and LUVs, respectively) fluorescently labeled at self-quenching concentrations, and the measured changes in bulk fluorescence is used as the fusion readout (7,19). In these assays, heterogeneities are hidden, information is averaged out, and fusion intermediates are not easily or directly assessed—membrane docking and adhesion are not detected because there are no associated changes in fluorescence. In addition, it is often difficult to translate (de)quenching kinetics into useful quantitative data, and results are prone to artifacts. Unequivocal assignment of docking, hemifusion, and full fusion was accomplished with membrane-covered beads of two different sizes (16). However, content mixing and membrane morphological changes after fusion were not accessible because of the hard beads as membrane support. Furthermore, most protein-mediated fusion experiments require protein reconstitution in liposomes containing 10–30 mol % of charged lipids (23–27). Presumably, this fraction is empirically chosen, but it is not clear whether the charges are important for the protein environment as a fusion mediator or even, as recently reported, for vesicle docking (28).

In contrast to conventional liposome-based assays used to study membrane fusion, direct imaging of the fusion process using giant unilamellar vesicles (GUVs) (29) has the potential to unravel useful information not accessible in bulk assays. With the use of GUVs, mechanical parameters recognized to modulate or be modified during the fusion process are potentially accessible, including changes in membrane tension, curvature, and elasticity as well as the molecular environment. Additionally, direct GUV observation potentially allows identification of fusion intermediates, detecting the area increase, and elevated probe concentration in the fusion region (e.g., in self-quenched membranes). Surprisingly, despite these advantages, not many studies report the use of GUVs in investigating processes associated with membrane fusion. These relatively few studies include the first direct visualization of a peptide-induced fusion (30) and formation of a hemifusion diaphragm (31), heated nanoparticle-mediated fusion (32), resolving the very fast nature of the fusion neck expansion on the order of  $\mu\text{m/s}$  (10) with rates depending on membrane properties (33), the role of regulatory proteins on SNARE-mediated fusion (34), and the effect of charge (35), multivalent ions (36), tension (37), and pH (38) on membrane fusion.

In this work, we introduce a protein-free GUV-LUV fusion system based on membranes of opposite charge and use a set of optical and mechanical methods for detailed investigation of the charge dependence of membrane fusion in a pure lipidic system. GUVs and LUVs closely mimic the curvature of the plasma membrane and fusion vesicles,

respectively. The system offers the additional advantage that fusion can be directly observed between freely diffusing LUVs and individual relatively immobile GUVs. To study the effects of membrane charge, we use cationic LUVs of a fixed composition and GUVs as a model cellular membrane with increasing (negative) charge density in the membrane by changing the ratio of charged lipids over zwitterionic lipids. For the cationic LUVs, we took inspiration from a lipid mixture containing a fluorescent lipid analog, which was demonstrated to quickly and spontaneously fuse with a number of cell lines, including those recognized to be difficult to transfect (39,40). This interaction has proven effective for the intracellular delivery of materials to which the cell membrane is otherwise impermeable (41,42). Importantly, these fusogenic liposomes constitute a promising carrier system because they are able to fuse with the plasma membrane and thus efficiently deliver the encapsulated cargo to the cytosol, and therefore they circumvent the usual low-efficiency endocytic routes of conventional liposomes. The method described here is based on real-time imaging and manipulation of GUVs upon fusion with LUVs. In particular, quantification of lipid mixing is achieved by evaluating the intensity- and lifetime-based fluorescence resonance energy transfer (FRET) efficiency between the acceptor dye present in the LUVs upon fusion with GUVs containing the donor dye. FRET values are translated to fusion efficiency and measured on individual single GUVs with increasing fractions of negative lipids. In combination with lipid dye quenching, vesicle electrodeformation, and vesicle mixing in a microfluidic device, we investigate how the membrane charge density on the GUVs controls the fusion efficiency and whether fusion proceeds leakage free.

## MATERIALS AND METHODS

The phospholipids 1-palmitoyl-2-oleoyl-*sn*-glycero-3-phosphocholine (POPC), 1-palmitoyl-2-oleoyl-*sn*-glycero-3-phospho-(1'-*rac*-glycerol) (sodium salt) (POPG), 1,2-dioleoyl-*sn*-glycero-3-phosphoethanolamine (DOPE), and 1,2-dioleoyl-3-trimethylammonium-propane (DOTAP); the fluorescent dye 1,2-dipalmitoyl-*sn*-glycero-3-phosphoethanolamine-N-(lissamine rhodamine B sulfonyl) (ammonium salt) (DPPE-Rh); and the headgroup-labeled 1,2-dipalmitoyl-*sn*-glycero-3-phosphoethanolamine-N-(7-nitro-2-1,3-benzoxadiazol-4-yl) (ammonium salt) (DPPE-NBD) were purchased from Avanti Polar Lipids (Alabaster, AL). Lipid solutions were prepared in chloroform and stored at  $-20^{\circ}\text{C}$  until use. Sulforhodamine B (SRB), sodium chloride (NaCl), calcium chloride ( $\text{CaCl}_2$ ), sucrose, glucose, and sodium dithionite were purchased from Sigma Aldrich (St. Louis, MO) and used as received. Low-melting temperature agarose was purchased from Thermo Fisher Scientific (Waltham, MA).

GUVs were formed by the electroformation method with few modifications (43); see [Supporting Materials and Methods](#). The vesicles were used fresh (the same day), and thus for vesicles made of POPC and POPG mixtures, slightly higher POPG concentration on the vesicle surface may be expected (44). Alternatively, the gel-assisted method (45) was used for GUVs with 100 mol% POPG. LUVs were produced by the extrusion method (41). For three-dimensional (3D) imaging, GUVs were immobilized in agarose 0.1% (w/v) (43). To quantify area increase upon fusion, GUVs were placed

on an electrofusion chamber (46) and connected to a function generator. For FRET imaging, vesicles were imaged with confocal microscopy in the sequential mode to minimize cross-talk for donor and acceptor excitation (Supporting Materials and Methods). NBD-PE donor and DPPE-Rh acceptor fluorescence were detected upon donor excitation. FRET was also followed using a microfluidic device; see Supporting Materials and Methods. GUVs were trapped in a polydimethylsiloxane-assembled chamber, and solutions and LUVs were flushed through the microchannels at 2  $\mu\text{L}/\text{min}$ . To distinguish hemifusion from full fusion, NBD transferred to GUVs was quenched with dithionite and added to the GUV-LUV mix in the presence of SRB (Supporting Materials and Methods). For FLIM (Supporting Materials and Methods), the FRET donor NBD-DPPE was excited by a pulsed diode laser with a 40 MHz repetition rate in the presence or absence of the FRET acceptor.

## RESULTS

We employed protein-free fusogenic liposomes (LUVs) composed of DOTAP/DOPE/dye, 1:1:0.1 (39,40) and GUVs primarily consisting of POPC with increasing molar fractions of POPG as a model of liposome-cell membrane fusion mediated by electrostatic interactions. Because the fusogenic liposomes already contain a lipid dye, they can be easily detected with fluorescence microscopy. Most of the results were obtained with LUVs labeled with DPPE-Rh (*red*; acceptor) as the fluorescent lipid dye and GUVs containing traces of NBD-PE (*green*; donor) because these fluorophores form a donor-acceptor FRET pair. Direct observation of GUVs enables detection of a number of distinct fusion intermediates such as membrane docking, hemifusion, and full fusion, as deduced from the morphological response of the GUVs and the fusion efficiency assessed from the measured FRET signal; see Fig. 1. In case of docking only, the LUVs adhere to the GUVs, which may be deformed because of the strong electrostatic interactions, but there is no or small associated FRET signal (Fig. 1, A and B). Upon hemifusion, the outer leaflet of GUVs contains the red dye from the hemifused LUVs, which can lead to a change in the color of the GUV and a low but detectable increase in FRET (Fig. 1 C); hemifusion can be also confirmed with quenching studies, as we will see further. Upon full fusion of the outer and inner leaflets of the two vesicles, a large amount of LUV lipids are transferred to

the GUV, increasing its area, and the associated changes in FRET are significantly higher because of the large transfer of the acceptor dye (Fig. 1 D). Because both LUV and GUV compositions (and their dye fractions) are known before fusion, the FRET signal can be quantitatively translated into fusion efficiency, and the membrane composition after fusion can be determined at the single-GUV level, as demonstrated below.

### Interaction of fusogenic LUVs with neutral and negative GUVs

Fusogenic LUVs (30  $\mu\text{M}$  lipid concentration) were incubated for 10–20 min with neutral POPC GUVs or negatively charged GUVs containing equimolar mixtures of POPC and POPG (the anionic fraction was chosen to approximately match the molar fraction of cationic lipids in the LUVs). Throughout the work, these GUVs are referred to as neutral and negative, respectively, unless mentioned otherwise. In the examples given below, we often make use of a protocol for GUV immobilization in 0.1–0.5 wt% agarose (43) to arrest the system for imaging and detect the fusion state (intermediates). The approach is based on building a “cage” around the GUV that stops its displacement, allowing for detailed 3D imaging, but leaves membrane fluctuations nearly unperturbed.

In samples of neutral GUVs, the LUVs appear stably docked to the membrane (adhered and diffusing across the GUV surface but not undocking); Fig. 2 A. A low but detectable amount of lipid transfer is also observed; see Supporting Materials and Methods. The LUVs are not visible in the NBD channel (Fig. S1), and therefore bleed-through is minimal, which is important for analyzing the FRET signal. The immobilization protocol was also used to very roughly quantify the number of docked LUVs on a single GUV; see Supporting Materials and Methods. On average, we found  $\sim 1$  stably docked LUV per  $\sim 5 \mu\text{m}^2$  of GUV surface. Interestingly, in a process similar to endocytosis, LUVs are often internalized into inward buds of neutral GUVs, in particular in vesicles exhibiting some excess area (Fig. 2 B), indicating possible changes in the GUV

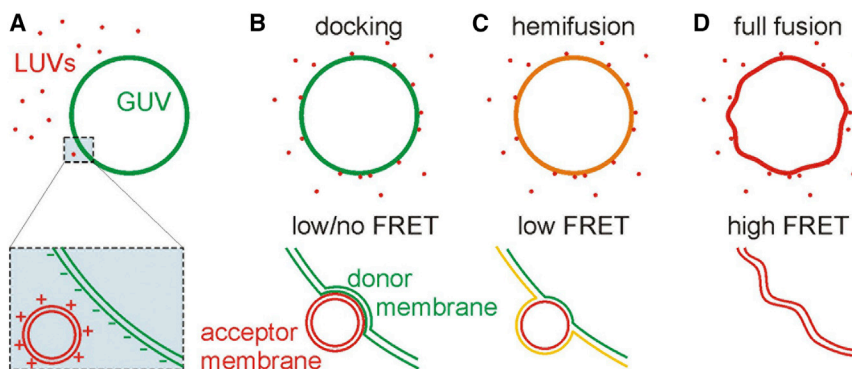
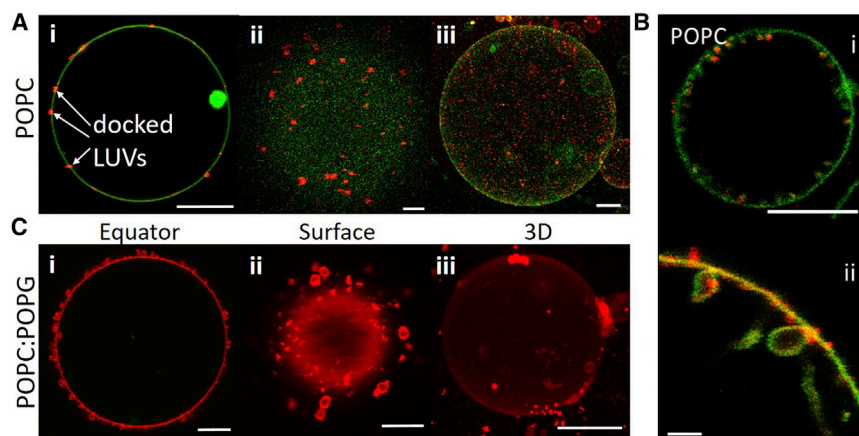


FIGURE 1 GUV-LUV fusion with associated observations of GUV morphology and FRET signal and their tentative interpretation. (A) GUVs containing the FRET donor (*green*) are incubated with fusogenic LUVs containing the FRET acceptor (*red*). (B–D) Schematics of the morphological and fluorescence changes accompanying the different fusion intermediates as directly observed under the microscope (*upper row*) and the associated leaflet rearrangement and FRET between the interacting pair for the respective intermediate (*lower row*). Fusion efficiency can be assessed from the measured FRET signal. To see this figure in color, go online.



**FIGURE 2** Different interactions of fusogenic LUVs with neutral (pure POPC) and negative (POPC/POPG 1:1) GUVs: (A) docking, (B) engulfment, and (C) full fusion. Images in (A) and (C) represent (i) equatorial cross sections, (ii) GUV top surface, and (iii) 3D reconstructions. In (A) and (B), the red dots correspond to docked LUVs, and images are overlays of NBD and rhodamine (Rh) direct excitation and emission. In (B), neutral GUVs engulf fusogenic LUVs: (i) a whole vesicle and (ii) a zoomed-in region. In (C), images show directly the FRET signal (NBD excitation and Rh detection). Images were contrast enhanced for better visualization (see also Fig. S1 for FRET signal from such vesicles). Vesicles were immobilized in agarose. Scale bars represent 10  $\mu\text{m}$ , except in (A(ii)), (B(ii)), and (C(ii)), where they represent 2  $\mu\text{m}$ . To see this figure in color, go online.

spontaneous curvature toward negative values (47). This can result from changes in membrane composition induced by asymmetric transfer of lipids (i.e., via hemifusion) and/or by LUV adhesion and engulfment coupled to membrane condensing effects by the charges on the LUVs. Although certainly interesting, the endocytosis-like process is out of the scope of this work.

In a striking contrast to neutral GUVs, incubation of LUVs with negative GUVs results in a massive transfer of lipids from LUVs to GUVs, as detected by the intense red fluorescence of the GUV surface (Fig. 2 C). The amount of transferred lipids is so high that the GUVs display large changes in their morphology, gaining a significant area stored in the form of membrane folds, buds, and tubes as discussed below.

### Real-time observation of GUV-LUV interaction: Membrane fusion increases GUV area

The results presented above were obtained after incubation of GUVs with the fusogenic LUVs and subsequent observation (imaging with and without GUV immobilization after incubation showed similar behavior). To reveal processes during the incubation, i.e., along the fusion pathway, we attempted to monitor in real time the interactions upon direct contact of the LUVs (30  $\mu\text{M}$  lipids) and GUVs. This was performed in different ways, and the results are summarized in Fig. 3. Initially, we observed the fusion process on negative GUVs trapped into a microfluidic chip, where the external solution could be exchanged almost instantaneously ( $\sim 400$  ms; see Supporting Materials and Methods; Video S1) using a technology developed previously (48,49). Differently from other microfluidic technology for observing membrane fusion events (14,50), here, we trapped single GUVs, and fusion was initiated by operating an integrated valve to controllably add a specific concentration of LUVs (see Supporting Materials and Methods for details). Our results obtained on chip suggest that fusion is fast, as shown in Fig. 3 A. Already in the first 30 s, a significant

decrease in NBD fluorescence due to FRET is seen. Structures inside the GUV remain inaccessible to the LUVs. The relative FRET efficiency ( $E_{FRET}$ ) was measured according to  $E_{FRET} = I_{Rh}/(I_{Rh} + I_{NBD})$ , where  $I_{Rh}$  and  $I_{NBD}$  are the respective Rh and NBD fluorescence intensities when only NBD is excited (51); see Supporting Materials and Methods. After  $\sim 100$  s,  $E_{FRET}$  is observed to reach a plateau approaching 1 (right panel in Fig. 3 A), which may result either from saturation of the fusion process and/or because of the definition of this quantity (for  $I_{Rh} \gg I_{NBD}$ ,  $E_{FRET}$  approaches 1 by default).

The microfluidic chip geometry and the flow applied to exchange the solution around the GUVs did not allow us to follow the associated morphological changes. We thus performed experiments in which a concentrated suspension of LUVs (30  $\mu\text{M}$  final lipid concentration after equilibration) was locally introduced in one corner of the observation chamber. The LUVs reach the GUVs by diffusion. Although kinetic information cannot be extracted in this experiment because LUV concentration close to a GUV at a given time cannot be precisely estimated, we could monitor the process from the beginning until equilibration (52). Fig. 3, B and C show respective sequences for a neutral and a negative GUV in the bulk interacting with LUVs. The starting times of the observations as indicated in the snapshots ( $t = 0$  s) is 10–30 s after mixing (note that vesicles located farther away from the place of LUV injection respond later). Initially, the neutral GUV is homogeneously fluorescent (green) and exhibits shape fluctuations, indicating that the vesicle is tensionless (Fig. 3 B, 15 s). As LUVs dock, the GUV changes its color, and its membrane fluctuations are suppressed (90 s) because of an increase in membrane tension (the volume remains constant as fusion proceeds without leakage, as discussed further below). Presumably, the vesicle excess area is consumed in the engulfment and wrapping of LUVs (see Fig. 2 B) as well as generating structures favoring negative spontaneous curvature (inward buds). Further docking/hemifusion (red spots visible on the GUV cross section at 320 s) results in



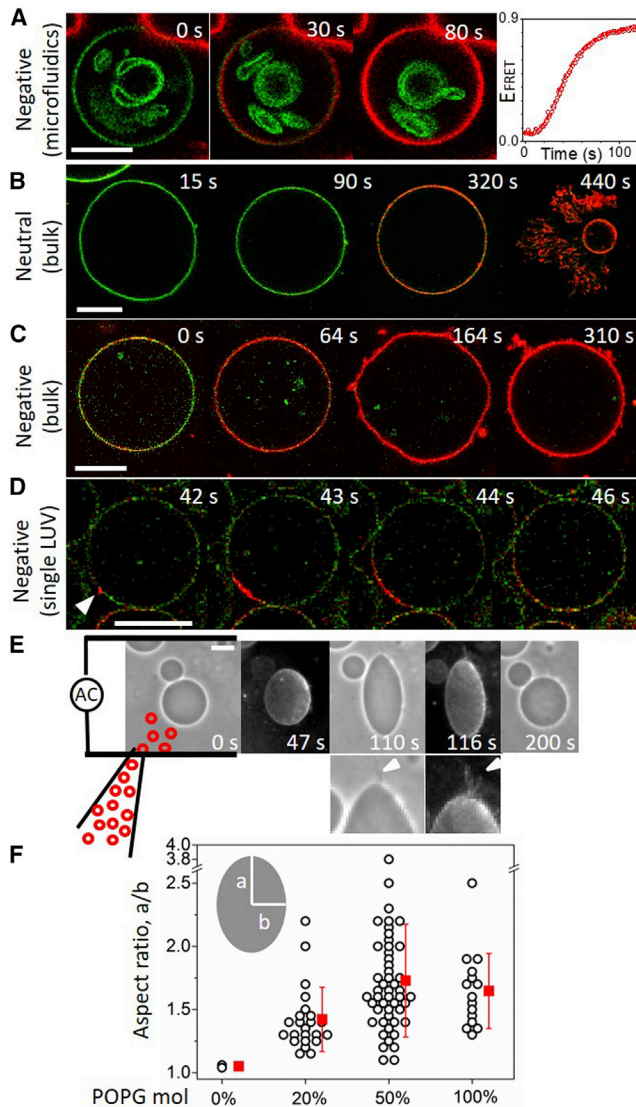


**FIGURE 3** GUV morphological transformations observed in real time upon addition of LUVs. (A–D) Confocal images of neutral and negative GUVs either trapped in a microfluidic device (A) or free floating in the bulk (B–D). Images are overlays of NBD and Rh direct excitation and emission. In (A), the external solution was fully exchanged with LUVs (30  $\mu$ M lipids) already in the first 400 ms. The NBD signal decreased, and the FRET increased, approaching 1 after  $\sim$ 100 s (figure on the right), whereas the internal structures in the GUV retain their green (NBD) intensity because they are not exposed to the LUV solution. The sequences (A–C) are shown in Videos S1 and S3. (D) A single LUV fusion event (acquisition was performed at higher frame rate resulting in lower signal/noise ratio). The time stamps in (B)–(D) indicate the time after initiating the observation on each vesicle. The arrowhead at 42 s in (D) points to the initially docked LUV, which becomes brighter as the partially self-quenched dye dequenches upon fusion, followed by a decrease as the dye is diluted. (E) Phase contrast and epifluorescence images of electrodeformation of a negative nonlabeled GUV under an AC field (100 V/cm, 100 kHz). The local injection of a concentrated LUV suspension (red circles) is schematically represented in the first snapshot. Zoomed regions below show lipid tubes (arrowheads), which form at the vesicle poles. The time stamps show time after LUVs are introduced in the chamber. The sequence is shown in Video S4. All scale bars represent 20  $\mu$ m. (F) Maximal aspect ratio  $a/b$  (as sketched in the inset) of electrodeformed GUVs upon LUV injection to final bulk concentration of 42 nM. Each point indicates a

additional tension and eventual vesicle rupture (440 s); note that the locally injected LUV concentration explored here is usually higher than that in the incubation experiments described above, which presumably causes the rupture. Similar behavior was observed with GUVs with low fraction of POPG (5 mol%). The vesicle bursting does not result from adhesion to the glass potentially mediated by LUVs because the GUV is observed to continually displace because of convection (see Video S2). The ruptured GUV restructures into a smaller vesicle containing nanotubes and buds dotted with red LUVs. We also observed LUV-mediated GUV-GUV adhesion and increase in tension, resulting in vesicle rupture (Fig. S6).

In sharp contrast, the interaction with the negative GUVs leads to a fast and efficient transfer of LUV lipids (Fig. 3 C; Video S3), as already suggested by the microfluidic experiments: the GUV is initially green (0 s—some fusion had occurred already before imaging started) and quickly acquires a strong DPPE-Rh fluorescence (64 s). Note that the Rh fluorescence is homogeneous over the GUV surface because docking is immediately followed by fusion. Further arrival of LUVs increases the vesicle fluctuation, indicating area gained by fusion (164 s). Eventually, the GUV returns to its quasispherical geometry, and the gained area is stored in the form of outward membrane folds, buds, and tubes (qualitatively similar formation of curved structures was previously observed upon fusion of a pair of GUVs (35)).

Interestingly, single fusion events can be also detected. Fig. 3 D shows a single LUV initially binding to and subsequently fusing with a negative GUV. At the dye concentration used ( $\sim$ 4.76 mol%), Rh fluorescence is partially self-quenched in the LUV. Thus, the single fusion events are characterized by a local increase in fluorescence resulting from initial lipid dilution (self-quenching is lost), followed by a decrease in fluorescence as the LUV lipids diffuse away from the fusion point and get diluted into the GUV membrane.

Morphologically, neutral GUVs that do not rupture are tense and spherical with many surface-docked LUVs and exhibit low to intermediate changes in color, whereas negative GUVs initially show large fluctuations as a result of area acquired from fusion with the LUVs and then gradually produce many membrane folds. To quantify the increase in area upon fusion, GUV-LUV interaction and fusion were followed in the presence of an AC electrical field. AC fields can be used to deform GUVs (53,54) and to assess changes in area (53–56), which can be translated into the amount of transferred lipids (i.e., upon fusion). We applied the AC field to initially spherical (little or no excess area) nonlabeled GUVs, and after the vesicle adopted its equilibrium shape as a result of electrodeformation, we locally injected labeled LUVs (0 s) with a pipette. The POPG molar ratio in the

single measurement on an individual GUV. Mean average and SDs are also indicated (red). To see this figure in color, go online.

GUVs was varied. Because at low POPG fractions, LUVs tend to disrupt the GUVs in the presence of the electric field, the final LUV concentration was decreased to 42 nM. The LUVs diffuse to the GUV, which starts to elongate (in the direction of the field) into a prolate shape (57). A typical sequence is shown in Fig. 3 E. The onset of deformation coincides with the appearance of Rh fluorescence in the GUV membrane (47 s) because deformation is coupled with fusion. Deformation proceeds up to a maximum (92 s for this particular GUV), after which the vesicle starts to emit membrane projections (tubes) at the vesicle poles facing the electrodes (110 s), easily observed by fluorescence (116 s—see insets in Fig. 3 D). Afterwards, the vesicle returns to its quasispherical shape (200 s), and the acquired area is stored in external buds and tubes. Importantly, the vesicle optical contrast due to the sugar asymmetry is preserved, indicating that the fusion process is not accompanied by changes in membrane permeability, i.e., it is leakage free.

The area gained from LUV fusion is not completely used for GUV deformation under an electric field (i.e., tube formation). Thus, we simply measured the maximal attained aspect ratio  $a/b$ ; see Fig. 3 F. Interaction of LUVs with neutral GUVs builds up tension in the membrane, leading to vesicle rupture. The very few GUVs that survived electrodeformation exhibited a negligible increase of the aspect ratio ( $a/b \sim 1$ ). In contrast, significant deformation occurs for vesicles containing POPG at or above 20 mol%. The increase levels out at 50 mol%.

### Full fusion versus hemifusion assay: Both are leakage-free processes

Whereas the morphological data presented above clearly demonstrate full fusion as the outcome of LUV interaction with GUVs at intermediate to high POPG fraction ( $\geq 20$  mol%), the data presented so far are inconclusive as to the pathway for GUVs at lower POPG fraction. Indeed, our data (showing a large number of docked LUVs, small but significant lipid transfer from docked LUVs, increase in membrane tension, and rupture) suggest that the process involves hemifusion, even though simple docking/adhesion with a low degree of full fusion cannot be ruled out. Distinguishing hemifusion (or even docking) from full fusion has proven to be a difficult task in both reconstituted and in vivo systems (25,58,59). Here, we take advantage of the fact that fluorescent dyes can be permanently quenched by specific molecules. In the presence of a membrane-impermeable quencher added externally to the GUVs, membrane fluorescence acquired from dye-labeled LUVs should be completely quenched when the dye is located exclusively in the outer GUV leaflet, whereas quenching should be on the order of 50% when the dye is symmetrically present in both leaflets. Here, we used the well-known quenching agent sodium dithionite (herein referred to as dithionite)

(60) for the selective quenching of NBD transferred from the LUVs to nonlabeled GUVs (see also (61) for dithionite permeability). Control experiments with NBD-labeled GUVs show that dithionite quenches  $\sim 50\%$  of the membrane fluorescence intensity (Fig. S7; Supporting Materials and Methods), corresponding to quenching exclusively the membrane outer leaflet. Because hemifusion of labeled LUVs with nonlabeled GUVs should transfer the dye only to the external GUV leaflet, we expect quenching to reduce the fluorescence by significantly more than 50% (the inner GUV leaflet would remain inaccessible to the quencher), as shown in control measurements (Fig. S8). If full fusion is the only pathway, ideally, only  $\sim 50\%$  quenching is expected. However, dithionite was often able to permeate the membranes in some cases, especially in POPC/POPG GUVs (see Fig. S9; Supporting Materials and Methods) and fusogenic LUVs (see Fig. S10; Supporting Materials and Methods). Therefore, dithionite was added after incubation of GUVs with LUVs to avoid transfer of dithionite from the inner volume of the LUVs to the interior of the GUVs when full fusion occurred. Additionally, the quenching experiments were carried out in the presence of the water-soluble dye SRB in the external medium to detect and exclude GUVs with compromised membrane integrity.

Fig. 4 A shows images of initially nonlabeled neutral GUVs incubated with NBD-labeled LUVs, which results in detectable lipid (NBD, green) transfer (Fig. 4 A, left),

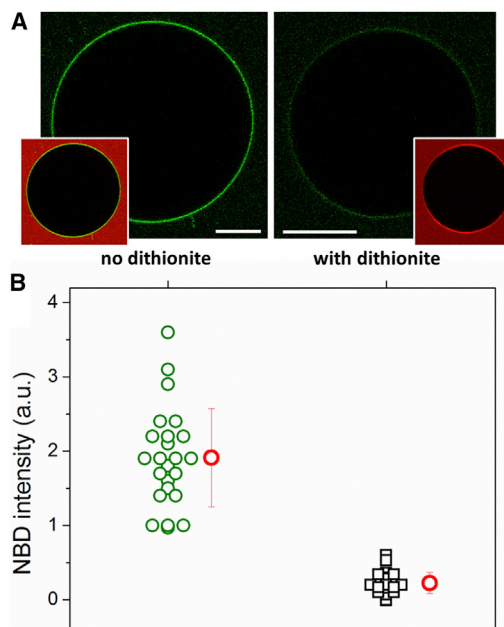


FIGURE 4 Quenching of NBD upon membrane fusion. (A) Images of nonlabeled POPC GUVs incubated with 1  $\mu\text{M}$  NBD-labeled LUVs (green) before (left) and after addition of 10 mM dithionite (right). Measurements were performed in the presence of 5  $\mu\text{M}$  SRB (red in inset), used to distinguish vesicles with noncompromised membranes. Scale bars represent 10  $\mu\text{m}$ . (B) NBD fluorescence intensity for the tested conditions. Each point represents a measurement on a single nonpermeable GUV. Mean average and SDs are also indicated (red). To see this figure in color, go online.

as already shown in Figs. 2 and 3. When 10 mM dithionite was added after incubation, the NBD fluorescence from the GUVs was almost completely suppressed (Fig. 4 A, right); the data for a large number of GUVs is shown in Fig. 4 B. The results show that NBD from fusogenic LUVs is transferred almost exclusively via hemifusion/docking to neutral membranes. Importantly, similarly to full fusion, the GUV integrity upon hemifusion is also preserved because SRB does not leak in, consistent with the preserved sugar contrast as observed in Fig. 3 E. To summarize, whereas fusogenic LUVs undergo full fusion with negative GUVs, the quenching experiments show that fusogenic LUVs undergo docking and predominantly hemifusion with neutral GUVs.

### A FRET-based single GUV assay: Assessing the membrane composition upon fusion

The LUV-GUV interaction was observed to depend on the fraction of the anionic POPG lipid in the GUVs (see Fig. 3 F). We speculated that the GUV surface charge controls not only the affinity to the LUV membranes but also determines whether interacting vesicles undergo docking/hemifusion or full fusion, as suggested by the quenching experiments. To unravel the role of membrane charge, we quantified the fusion efficiency for varying fractions of POPG in the GUVs. To this end, we developed a single GUV-based FRET assay using DPPE-Rh-labeled LUVs and DPPE-NBD-labeled GUVs; see [Supporting Materials and Methods](#). Fusion results in transfer of DPPE-Rh from LUVs to GUVs and therefore increases FRET efficiency. Lipid transfer can be detected via Rh emission through NBD excitation. To relate FRET to fusion efficiency and to assess the compositional change in the GUVs resulting from fusion, we constructed a calibration curve based on FRET signal detected in POPC GUVs containing a fixed amount of NBD (0.5 mol%, as in the fusion experiments) and increasing concentration of Rh (0–5 mol%); see [Supporting Materials and Methods](#) and Fig. S5. The FRET signal for the calibration curve did not appear to depend on the presence of charged lipid or salt (data not shown). Because absolute FRET efficiencies depend on different parameters sometimes difficult to measure (i.e., the dipole orientation of the donor emission and acceptor absorption), the data presented here are sensitive within the range of donor/acceptor dye ratios used in the calibration. The advantages of using a FRET-based assay over a single-dye assay (i.e., detecting the signal from labeled LUVs fusing to nonlabeled GUVs) are manifold: the possibility to observe GUVs before (and after) fusion by fluorescence, improved sensitivity of FRET-based assays, and the detection of fusion intermediates (i.e., distinguishing docking from hemi- or full fusion).

Results from the incubation of LUVs with GUVs of increasing POPG mol% are shown in Fig. 5 A, with the respective measured  $E_{FRET}$  values. Note that being initially

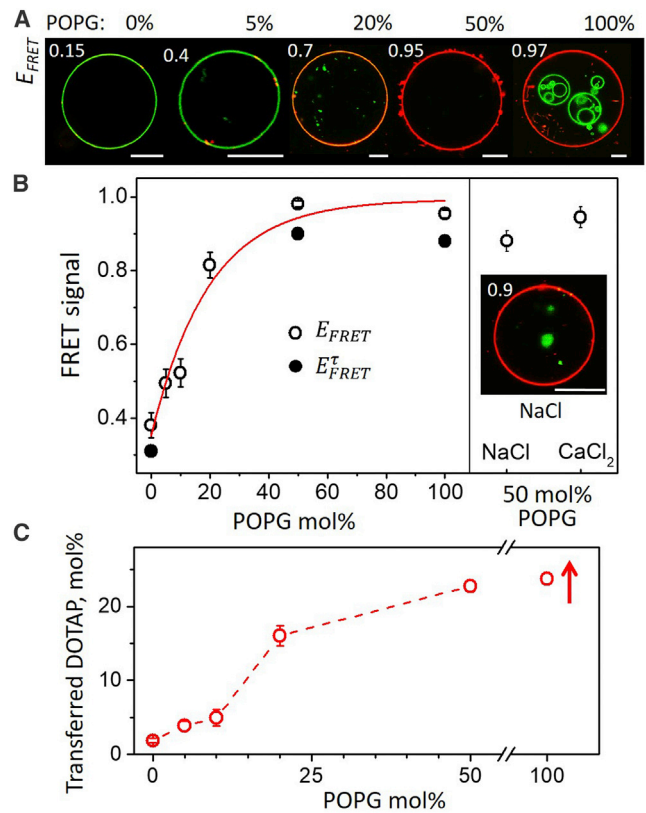


FIGURE 5 FRET-based assay for deducing the GUV membrane composition after fusion. (A) Confocal cross sections of different GUVs at increasing POPG molar fractions (indicated above each snapshot) incubated with LUVs (30  $\mu$ M lipid). Images are overlays of NBD and Rh sequential direct excitation and emission and FRET channel; see [Supporting Materials and Methods](#). The respective  $E_{FRET}$  values are shown in the upper left corner. (B) Average intensity-based FRET,  $E_{FRET}$ , for GUVs of increasing POPG molar fractions (open circles); data from 25 to 40 GUVs per composition. The exponential fit (red curve) is a guide to the eye. FLIM-FRET data,  $E_{FRET}^f$  (solid circles), are included for comparison; see main text and [Supporting Materials and Methods](#) for details. The right segment shows  $E_{FRET}$  measured for GUVs containing 50 mol% POPG in the presence of 100 mM NaCl or 5–50 mM  $CaCl_2$ . The inset shows one GUV in the presence of NaCl with  $E_{FRET}$  value indicated on the image. Scale bars represent 10  $\mu$ m. (C) Fraction of DOTAP in the GUVs after fusion for increasing POPG molar fraction in the membrane as deduced from the  $E_{FRET}$  values, see text. Upward arrow indicates possible underestimation of the measured parameters for 100 mol% POPG GUVs; see text for details. Error bars in (B) and (C) indicate standard errors. To see this figure in color, go online.

green, the GUVs display more DPPE-Rh fluorescence for increasing POPG mol%. Importantly, fusion is restricted to the bilayers in contact because vesicles inside GUVs are protected from interaction and fusion with LUVs (see Fig. 3 A and the GUV image for POPG 100 mol% in Fig. 5 A).  $E_{FRET}$  values measured on a number of GUVs of different compositions are shown in Fig. 5 B. At low POPG fraction ( $\leq 10$  mol%),  $E_{FRET}$  is low (0.35–0.5), and many LUVs are observed on the GUV surface (diffraction-limited spots), suggesting hemifusion and docking. Increasing POPG to 20 mol% results in a twofold increase



in  $E_{FRET}$ . Deformation data (Fig. 3) show that at this fraction, interaction results in full fusion. Therefore, transition from mainly hemifusion to (predominantly) full fusion occurs between 10 and 20 mol% POPG. Standard error rather than SD is shown for clarity because of the large scatter at low POPG fractions, which could result from compositional heterogeneity of the prepared GUVs (62) and other factors discussed in more detail in [Supporting Materials and Methods](#). Increasing POPG to 50 mol% and above results in further increase and saturation of  $E_{FRET}$  ( $\sim 1$ ). This could be interpreted as a result of charge compensation because the amount of cationic DOTAP transferred to GUVs via fusion equals the amount of anionic POPG, and fusion no longer proceeds. However, we suspect that saturation in  $E_{FRET}$  also arises because, by definition, this quantity approaches 1 for  $I_{Rh} \gg I_{NBD}$ . In any case, data are less scattered at high POPG fractions also because the electrostatic interaction is more pronounced. Variations in the FRET signal can only be detected because individual GUVs are probed (see Fig. S11), and this is in sharp contrast with bulk assays in which only average values are gathered, potentially including signal from ruptured membranes.

The driving force of fusion in the system is clearly of an electrostatic nature. Therefore, it is plausible that fusion might be influenced by screening of the charges by salt. We incubated LUVs and negative GUVs dispersed in salt solutions of monovalent (100 mM NaCl) or divalent (5–50 mM CaCl<sub>2</sub>) ions. Osmotic imbalance from the added salts was circumvented by reducing sugar concentrations accordingly. In these conditions, vesicle aggregation and adhesion were observed, and the vesicles exhibited surface defects and folds; we examined only nonadhering, defect-free portions of the GUVs. In both cases, fusion was as efficient as in the pure sugar solution, as shown in Fig. 5 B (see Fig. S12 for data from individual vesicles), with measured  $E_{FRET}$  close to 1. Although somewhat unexpected, these results are not completely surprising. Other charge-mediated membrane fusion assays have reported little or no effects of a range of salts on fusion of charged membranes (63–65). For the conditions described here, electrostatic interactions between membranes of opposite charges are so strong that the presence of these ions was not able to affect fusion at a detectable level. Presumably, the effect of salt will be more pronounced for lower POPG fractions in the GUV membrane, which we are currently exploring.

An important advantage of the FRET assay we have developed is that it allows us to assess the GUV final composition after fusion with LUVs. From the calibration curve (Fig. S5) and the value of  $E_{FRET}$  measured on GUVs that have undergone fusion, we can deduce the resulting Rh/NBD dye ratio and thus assess how many of the LUV lipids have been transferred to the GUV. The NBD amount on the GUV is fixed for the various fractions of POPG, whereas the amount of transferred Rh is proportional to that of DOTAP from the fusing LUVs. Thus, the final

GUV composition upon fusion can be directly estimated from the Rh/NBD dye ratio; calculations are detailed in [Supporting Materials and Methods](#). In Fig. 5 C, we show the final DOTAP fraction reached in the GUV membrane upon fusion. At low POPG fractions, at which docking and hemifusion dominate, the amount of transferred DOTAP is small, below 5 mol%. However, for GUVs with 20 mol% POPG, the amount of transferred DOTAP increases significantly and levels out for GUVs with  $\geq 50$  mol% POPG. Because fusion of LUVs results in dilution of the GUV lipids, for a GUV initially containing 50 mol% POPG, the increase of DOTAP fraction to around 23 mol% (Fig. 5 C) would imply a  $\sim 1:1$  final ratio of positive/negative charges, i.e., neutralization. However, this saturation may be an artifact from the reduced sensitivity at  $E_{FRET}$  values approaching 1 (indicated with a red upward arrow in Fig. 5 C for 100% POPG); note that because of the definition of this quantity (as long as  $I_{Rh} \gg I_{NBD}$ ,  $E_{FRET}$  approaches 1 by default), the sensitivity to transferred DOTAP is reduced.

To roughly test the validity of our assessment for the final GUV composition after fusion, we prepared vesicles with composition approximating the final predicted GUVs after fusion. Measurements of the diffusion coefficient of these mimetic systems were consistent with measurements on GUVs after fusion; see [Supporting Materials and Methods](#) corroborating our findings for the membrane composition of the fused vesicles.

### FLIM-FRET measurements of GUV-LUV fusion

Intensity-based FRET measurements are prone to artifacts (66), including decreases in signals due to photobleaching or changes in dye concentrations, the latter of which could affect the  $E_{FRET}$  calculations above if the donor dye is significantly diluted upon fusion. Therefore, we performed similar experiments on GUV-LUV fusion using fluorescence lifetime imaging microscopy (FLIM) and calculated the resulting FLIM-FRET efficiencies ( $E_{FRET}^T$ ). Measurements involving fluorescence lifetimes do not suffer from the above intensity-based issues and as the FRET efficiencies can be calculated directly, there is no need for a calibration curve. Here, the donor DPPE-NBD lifetime ( $\tau$ ) was measured in the absence and presence of the acceptor DPPE-Rh before ( $\tau_{before}$ ) and after ( $\tau_{after}$ ) fusion, respectively. We performed FLIM-FRET measurements for increasing POPG mol% as a further validation of the intensity-based FRET; see [Supporting Materials and Methods](#). Before fusion, the average lifetime of DPPE-NBD  $\tau_{before}$  in POPC GUVs is 7.74 ns and slightly lower for negative GUVs (6.49 and 6.59 ns for vesicles containing, respectively, 50 and 100 mol% POPG). Upon fusion with LUVs, the dye lifetime decreases (because of FRET) in a manner that depends on GUV charge: whereas for the neutral POPC, the decrease in lifetime is moderate

( $\tau_{after} = 5.34$  ns), it is strongly reduced for GUVs containing 50 and 100 mol% POPG ( $\tau_{after} = 0.59$  and 0.80 ns, respectively) because of very efficient FRET, as a result of significant fusion. All values are displayed in Table S2.

From the measured NBD membrane lifetimes before and after fusion, it is possible to calculate the absolute FRET efficiencies using  $E_{FRET}^T = 1 - \tau_{after}/\tau_{before}$ . The data are displayed in Fig. 5 B; see also Fig. S14. Even though the  $E_{FRET}^T$  values obtained from FLIM images are quantitative rather than the relative FRET values taken from the intensity-based approach, it is still not possible to draw further conclusions regarding charge neutralization with pure POPG GUVs. This is due to the limitations of measuring the very short fluorescence lifetimes of DPPE-NBD resulting from extremely efficient fusion. Nevertheless, the FLIM-FRET data strongly agree with data from intensity-based FRET, highlighting the robustness of the charge-mediated GUV-LUV fusion assay.

## DISCUSSION

We have developed a protein-free GUV-LUV fusion system based on the interaction of membranes of opposite charge. Quantitative GUV imaging and manipulation allowed determination of the charges that control the well-defined fusion intermediate transitions at the level of single vesicles. The way cationic fusogenic LUVs interact with GUVs is determined by the charge density of the GUV membrane, here controlled by the molar fraction of the anionic lipid POPG. At low POPG fraction, LUVs stably dock to the GUV surface and undergo diffusional mobility. Such interaction results in low but detectable lipid transfer via membrane hemifusion and asymmetric lipid transfer to GUVs, leading to increase in their membrane curvature and tension and eventually causing rupture. In sharp contrast, the number of stably docked LUVs is much lower for the negatively charged GUVs because docking is immediately followed by fusion to membranes with intermediate to high POPG molar fraction ( $\geq 20$  mol%). This results in massive lipid transfer via full fusion, leading to pronounced in-

crease in vesicle area together with monolayer area asymmetry inherently present on the LUVs (as discussed below and illustrated in Fig. 6) and an increase in spontaneous tension.

The induced membrane tension, which is evident from reduced membrane fluctuations (in the absence of electric field) or acting against electrodeformation and decreasing the aspect ratio  $a/b$  (both shown in Fig. 3), can be caused by two factors: 1) LUV adhesion in the case of neutral GUVs and 2) fusion in the case of the charged GUVs. In the first case, the GUV excess membrane (initially stored in fluctuations) is consumed by the adhering vesicles, which might get engulfed (Fig. 2 B), or by hemifusion. In the second case, because of the small size ( $\sim 70$  nm in radius as measured with dynamic light scattering; Supporting Materials and Methods), the fusing LUVs are characterized by a difference in the areas of their membrane leaflets (the outer leaflet area is larger by  $\sim 5\%$ ). Upon hemifusion and full fusion, the leaflets of the GUVs increase asymmetrically in area (the outer leaflet acquiring more lipids), which induces a positive spontaneous curvature (67,68), as schematically illustrated in Fig. 6. This in turn leads to the generation of highly curved protrusions (nanotubes and buds) and an increase in the spontaneous tension (69,70). As a result, the projected area of the vesicle decreases. In a similar system, an increase in GUV area upon fusion was observed, followed by the formation of dense lipid aggregates at the GUV surface rather than membrane tubes (71).

Under an AC field, the produced tubular structures are located predominantly at the vesicle poles facing the electrodes (see Figs. 3 E and 6), compared to tubulation over the whole vesicle surface in the absence of the field (Fig. 3 C). This could be due to 1) the higher local curvature at the poles of the elliptical GUV facilitating the tube formation and 2) field-induced accumulation of charged lipids in this region, leading to locally enhanced fusion efficiency and increased spontaneous curvature. Similar behavior was observed recently on electrodeformed GUVs doped with light-responsive molecules (72).

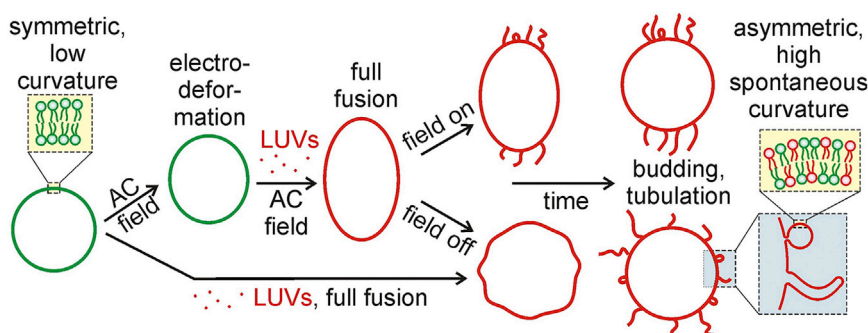


FIGURE 6 Morphological transformations associated with changes in curvature upon full fusion. An initially flat GUV membrane has almost zero membrane (spontaneous) curvature and is amenable to deformation under an AC field. An initial increase in vesicle area resulting from fusion with LUVs (red dots) is observed as an increase in GUV deformation under an AC field (upper pathway) or as an increase in membrane fluctuations in the absence of an AC field (lower path). In the former case, the curved structures are aligned with the field direction. The LUVs, inherently bearing a leaflet area asymmetry (more lipids are present in their outer leaflet), impart this

asymmetry to the GUVs upon fusion. The GUV membrane acquires a higher fraction of LUV lipids in its external leaflet, inducing positive spontaneous curvature, which stabilizes highly curved outward tubes and buds. To see this figure in color, go online.

The spontaneous curvature  $m$  resulting from the GUV membrane asymmetry acquired during fusion with the LUVs (Fig. 6) acts to generate tension (spontaneous tension)  $\sim 2\kappa m^2$ , where  $\kappa$  is the membrane bending rigidity ( $\kappa \sim 3.6 \times 10^{-20}$  J, as reported for membranes doped with POPG (73)). Because the elliptical deformation as induced by the electric field is suppressed during fusion, we can assume that the generated spontaneous tension, which brings back the vesicle to a sphere, is higher than the electric-field tension. The latter can be roughly estimated from the vesicle shape (before the onset of fusion) and field amplitude (74) and in our experiments is on the order of  $10^{-2}$   $\mu\text{N/m}$ . This implies that the lower limit of the spontaneous tension is of similar magnitude. Thus, the corresponding spontaneous curvature induced during fusion is at least on the order of  $1/(2.6 \mu\text{m})$ . This implies that the diameter of the produced buds and tubes is in the (sub)micron range (for small buds and necklace tubes, the spontaneous curvature is  $m = 1/R_{sph}$ , where  $R_{sph}$  is the radius of the spheres or the bud; for cylindrical tubes with radius  $R_{cyl}$ ,  $m = 0.5/R_{cyl}$ ). Indeed, the initial tubes that are observed protruding at the poles of the vesicles during electrodeformation (see Fig. 3 E; Video S4) have these diameters and seem to become thinner and with diameters not optically resolvable as fusion proceeds further. The exact change in the membrane spontaneous curvature can be assessed with tube-pulling experiments (70) or micropipette aspiration (75) and remains to be confirmed. Presumably, lipid flip-flop over time would allow for relaxing the spontaneous curvature acquired from fusion.

To measure fusion efficiency, we developed a quantitative FRET-based assay that enables measurements on a single-GUV level. Construction of a calibration curve with a controlled ratio of fluorescent donor and acceptor dyes allowed assessing the changes in membrane composition from measurements of intensity-based FRET ( $E_{FRET}$ ) in fused GUVs. The fusion efficiency as assessed from intensity-based FRET was further validated with FLIM-FRET ( $E_{FRET}^f$ ). We showed that membrane charge is the driving force for fusion and controls the transition from docking/hemifusion to full fusion. In the high FRET regime, even though both intensity and lifetime-based FRET lose sensitivity (and the ability to determine membrane compositional changes), mechanical deformation of GUVs under an electrical field showed that the degree of deformation for pure POPG GUVs is similar to that of GUVs containing 50 mol% POPG. This may suggest saturation of the fusion process and that charges are only partially neutralized in pure POPG GUVs. However, GUV electrodeformation does not show the full area gain resulting from fusion because of the imposed spontaneous tension stemming from the acquired asymmetry between the membrane leaflets. As a consequence, the degree of deformation is a balance between fusion efficiency (which favors deformation) and spontaneous tension (which suppresses deformation).

Therefore, it remains unclear whether charges on pure POPG GUVs are also neutralized.

The charge-dependent fusion system described here recapitulates all fusion steps observed with protein-reconstituted systems (i.e., SNARE fusion), and the fusion efficiency is as high as or higher than most reconstituted systems described in the literature. For example, SNARE-only liposomes are shown to result simply in hemifusion, whereas full fusion requires additional regulatory proteins (76,77). The dependence of the transition of fusion intermediates from docking to hemifusion as a function of POPG fraction is reminiscent of that in SNARE-reconstituted systems in which transitions also depend on SNARE density (8). In terms of POPG molar fraction, hemifusion to full fusion occurs at 10–20 mol% POPG, and saturation occurs at 50 mol% POPG or above. These conditions result in a final DOTAP fraction in the GUV from below 5 to near 25% after hemifusion and full fusion, respectively. None of the results are influenced by mono- and divalent ions such as  $\text{Na}^+$  and  $\text{Ca}^{+2}$ , and in contrast to other systems (78–80), both docking/hemifusion and full fusion are leakage free. Moreover, fusion proceeds with kinetics faster than most SNARE systems even in the presence of regulatory proteins (21,23,25,34,76,77,81).

The GUV-LUV fusion system explored here does not allow for fully resolving the kinetics of (single) fusion events, as is the case for systems employing membrane patches or supported bilayers using total internal reflectance fluorescence microscopy (82–84). However, our approach allows for distinguishing whether fusion proceeds leakage-free, overcomes effects associated with membrane tension, and allows for assessing the area growth and associated curvature affects.

We observed a large variation in fusion efficiency among vesicles of a given composition, especially for low POPG fractions. This can result from 1) membrane compositional heterogeneity and 2) variations in surface tension. Indeed, recent observations by us point to variations in the molar fraction of charged lipids among different electroformed GUVs (R.B. Lira, R. Dimova, K.A. Riske, unpublished data; see also (44)). This effect is negligible for high POPG mol%, at which fusion is very efficient. However, it is very pronounced for lower POPG fractions (10–20 mol%) at which transition from hemifusion to full fusion is observed. In addition, membrane tension varies by orders of magnitude among different vesicles in the same sample, from  $10^{-9}$  to  $10^{-3}$  N/m (46,71,85). Membrane tension is known to regulate fusion (37,86,87), and such large variations in tension among different GUVs certainly affects the fusion efficiency, especially at low POPG molar fractions.

The LUV membrane composition contains nearly 50 mol% of DOPE, a lipid with a preferred negative curvature and a tendency to form hexagonal phases (88). This explains the strong efficiency of PE-containing liposome formulations to fuse with cells and the associated higher



drug and/or nucleotide delivery efficiency when compared to lipids with lamellar phase preference. The different effects of membrane charge density and phase preference also controls the trafficking route of hexagonal or lamellar phase liposomes into cells (89). Switching the delivery route from endocytosis to direct fusion with the plasma membrane would increase both delivery speed and efficiency, circumventing the limiting barriers associated with intracellular trafficking and potentially decreasing transfection cytotoxicity. Direct fusion is indeed an efficient way to transfer materials of a wide range of sizes and physical-chemical properties directly into the cell cytosol (42). Importantly, the fact that the fusion efficiency is increased with anionic membranes could help target the enclosed therapeutic substances in fusogenic liposomes to tumor cells, which expose a significant fraction of the anionic lipid phosphatidylserine. Understanding the role of membrane charge density and how it controls the transition of fusion intermediates will certainly improve the development of lipid-based transfection reagents in therapy and drug delivery with higher efficiency and fewer side effects, a long-term goal in medical and biotechnological fields (90).

Direct observation of LUVs and GUVs enables the measurement of a number of mechanical properties (i.e., tension, curvature, elasticity) or molecular parameters (i.e., diffusion coefficient, lipid order) that are modified during the evolution of fusion and its intermediates. We envisage that our approach could be easily adapted to the study of fusion with SNARE-reconstituted vesicles in the presence of accessory proteins and thus resolve how accessory proteins or other fusogens influence each intermediate independently. Single-GUV observation and manipulation have the additional advantage that these properties can be measured or changed in real time for the very same vesicle, an approach that is not possible with any other fusion assay.

## SUPPORTING MATERIAL

Supporting Materials and Methods, 14 figures, two tables, and four videos are available at [http://www.biophysj.org/biophysj/supplemental/S0006-3495\(18\)34450-3](http://www.biophysj.org/biophysj/supplemental/S0006-3495(18)34450-3).

## AUTHOR CONTRIBUTIONS

The manuscript was written through contributions of all authors. All authors have given approval to the final version of the manuscript.

## ACKNOWLEDGMENTS

We thank J. Steinkühler for the help in designing the intensity FRET assay. R.B.L. thanks Rafaela Cavalcanti for her help with sample preparations.

This work is part of the MaxSynBio consortium, which was jointly funded by the Federal Ministry of Education and Research of Germany and the

Max Planck Society. The financial support of Fapesp is acknowledged (process numbers 11/22171-6, 13/07246-5, and 16/13368-4).

## REFERENCES

- Martens, S., and H. T. McMahon. 2008. Mechanisms of membrane fusion: disparate players and common principles. *Nat. Rev. Mol. Cell Biol.* 9:543–556.
- Jahn, R., T. Lang, and T. C. Südhof. 2003. Membrane fusion. *Cell.* 112:519–533.
- Chernomordik, L. V., and M. M. Kozlov. 2008. Mechanics of membrane fusion. *Nat. Struct. Mol. Biol.* 15:675–683.
- Jahn, R., and R. H. Scheller. 2006. SNAREs—engines for membrane fusion. *Nat. Rev. Mol. Cell Biol.* 7:631–643.
- Wickner, W., and R. Schekman. 2008. Membrane fusion. *Nat. Struct. Mol. Biol.* 15:658–664.
- Gong, B., B. K. Choi, ..., K. Kim. 2015. High affinity host-guest FRET pair for single-vesicle content-mixing assay: observation of flickering fusion events. *J. Am. Chem. Soc.* 137:8908–8911.
- Marsden, H. R., I. Tomatsu, and A. Kros. 2011. Model systems for membrane fusion. *Chem. Soc. Rev.* 40:1572–1585.
- Lu, X., F. Zhang, ..., Y. K. Shin. 2005. Membrane fusion induced by neuronal SNAREs transits through hemifusion. *J. Biol. Chem.* 280:30538–30541.
- Kim, J. Y., B. K. Choi, ..., N. K. Lee. 2012. Solution single-vesicle assay reveals PIP2-mediated sequential actions of synaptotagmin-1 on SNAREs. *EMBO J.* 31:2144–2155.
- Haluska, C. K., K. A. Riske, ..., R. Dimova. 2006. Time scales of membrane fusion revealed by direct imaging of vesicle fusion with high temporal resolution. *Proc. Natl. Acad. Sci. USA.* 103:15841–15846.
- Yang, P., R. Lipowsky, and R. Dimova. 2009. Nanoparticle formation in giant vesicles: synthesis in biomimetic compartments. *Small.* 5:2033–2037.
- Steubing, R. W., S. Cheng, ..., M. W. Berns. 1991. Laser induced cell fusion in combination with optical tweezers: the laser cell fusion trap. *Cytometry.* 12:505–510.
- Bahadori, A., L. B. Oddershede, and P. M. Bendix. 2017. Hot-nanoparticle-mediated fusion of selected cells. *Nano Res.* 10:2034–2045.
- Bahadori, A., G. Moreno-Pescador, ..., P. M. Bendix. 2018. Remotely controlled fusion of selected vesicles and living cells: a key issue review. *Rep. Prog. Phys.* 81:032602.
- Robson Marsden, H., N. A. Elbers, ..., A. Kros. 2009. A reduced SNARE model for membrane fusion. *Angew. Chem. Int.Engl.* 48:2330–2333.
- Bao, C., G. Pähler, ..., A. Janshoff. 2013. Optical fusion assay based on membrane-coated spheres in a 2D assembly. *J. Am. Chem. Soc.* 135:12176–12179.
- Lentz, B. R. 2007. PEG as a tool to gain insight into membrane fusion. *Eur. Biophys. J.* 36:315–326.
- Yaroslavov, A. A., A. V. Sybachin, ..., F. M. Menger. 2011. Liposome fusion rates depend upon the conformation of polycation catalysts. *J. Am. Chem. Soc.* 133:2881–2883.
- Struck, D. K., D. Hoekstra, and R. E. Pagano. 1981. Use of resonance energy transfer to monitor membrane fusion. *Biochemistry.* 20:4093–4099.
- Loyter, A., V. Citovsky, and R. Blumenthal. 1988. The use of fluorescence dequenching measurements to follow viral membrane fusion events. *Methods Biochem. Anal.* 33:129–164.
- Martens, S., M. M. Kozlov, and H. T. McMahon. 2007. How synaptotagmin promotes membrane fusion. *Science.* 316:1205–1208.
- Chan, Y. H., B. van Lengerich, and S. G. Boxer. 2009. Effects of linker sequences on vesicle fusion mediated by lipid-anchored DNA oligonucleotides. *Proc. Natl. Acad. Sci. USA.* 106:979–984.

23. McNew, J. A., F. Parlati, ..., J. E. Rothman. 2000. Compartmental specificity of cellular membrane fusion encoded in SNARE proteins. *Nature*. 407:153–159.
24. Karatekin, E., J. Di Giovanni, ..., J. E. Rothman. 2010. A fast, single-vesicle fusion assay mimics physiological SNARE requirements. *Proc. Natl. Acad. Sci. USA*. 107:3517–3521.
25. Cypionka, A., A. Stein, ..., P. J. Walla. 2009. Discrimination between docking and fusion of liposomes reconstituted with neuronal SNARE-proteins using FCS. *Proc. Natl. Acad. Sci. USA*. 106:18575–18580.
26. Witkowska, A., and R. Jahn. 2017. Rapid SNARE-mediated fusion of liposomes and chromaffin granules with giant unilamellar vesicles. *Biophys. J.* 113:1251–1259.
27. Kuhlmann, J. W., M. Junius, ..., C. Steinem. 2017. SNARE-mediated single-vesicle fusion events with supported and freestanding lipid membranes. *Biophys. J.* 112:2348–2356.
28. Lou, X., J. Kim, ..., Y. K. Shin. 2017.  $\alpha$ -Synuclein may cross-bridge v-SNARE and acidic phospholipids to facilitate SNARE-dependent vesicle docking. *Biochem. J.* 474:2039–2049.
29. Dimova, R., S. Aranda, ..., R. Lipowsky. 2006. A practical guide to giant vesicles. Probing the membrane nanoregime via optical microscopy. *J. Phys. Condens. Matter*. 18:S1151–S1176.
30. Kahya, N., E. I. Pêcheur, ..., D. Hoekstra. 2001. Reconstitution of membrane proteins into giant unilamellar vesicles via peptide-induced fusion. *Biophys. J.* 81:1464–1474.
31. Nikolaus, J., M. Stöckl, ..., A. Herrmann. 2010. Direct visualization of large and protein-free hemifusion diaphragms. *Biophys. J.* 98:1192–1199.
32. Rørvig-Lund, A., A. Bahadori, ..., L. B. Oddershede. 2015. Vesicle fusion triggered by optically heated gold nanoparticles. *Nano Lett.* 15:4183–4188.
33. Riske, K. A., N. Bezlyepkina, ..., R. Dimova. 2006. Electrofusion of model lipid membranes viewed with high temporal resolution. *Biophys. Rev. Lett.* 1:387–400.
34. Taresté, D., J. Shen, ..., J. E. Rothman. 2008. SNAREpin/Munc18 promotes adhesion and fusion of large vesicles to giant membranes. *Proc. Natl. Acad. Sci. USA*. 105:2380–2385.
35. Lei, G., and R. C. MacDonald. 2003. Lipid bilayer vesicle fusion: intermediates captured by high-speed microfluorescence spectroscopy. *Biophys. J.* 85:1585–1599.
36. Tanaka, T., and M. Yamazaki. 2004. Membrane fusion of giant unilamellar vesicles of neutral phospholipid membranes induced by La<sup>3+</sup>. *Langmuir*. 20:5160–5164.
37. Kliesch, T. T., J. Dietz, ..., A. Janshoff. 2017. Membrane tension increases fusion efficiency of model membranes in the presence of SNAREs. *Sci. Rep.* 7:12070.
38. Trier, S., J. R. Henriksen, and T. L. Andresen. 2011. Membrane fusion of pH-sensitive liposomes – a quantitative study using giant unilamellar vesicles. *Soft Matter*. 7:9027–9034.
39. Csiszár, A., N. Hersch, ..., B. Hoffmann. 2010. Novel fusogenic liposomes for fluorescent cell labeling and membrane modification. *Bioconjug. Chem.* 21:537–543.
40. Kleusch, C., N. Hersch, ..., A. Csiszár. 2012. Fluorescent lipids: functional parts of fusogenic liposomes and tools for cell membrane labeling and visualization. *Molecules*. 17:1055–1073.
41. Lira, R. B., M. A. B. L. Seabra, ..., A. Fontes. 2013. Studies on intracellular delivery of carboxyl-coated CdTe quantum dots mediated by fusogenic liposomes. *J. Mater. Chem. B*. 1:4297–4305.
42. Kube, S., N. Hersch, ..., A. Csiszár. 2017. Fusogenic liposomes as nanocarriers for the delivery of intracellular proteins. *Langmuir*. 33:1051–1059.
43. Lira, R. B., J. Steinkühler, ..., K. A. Riske. 2016. Posing for a picture: vesicle immobilization in agarose gel. *Sci. Rep.* 6:25254.
44. Steinkühler, J., P. De Tillieux, ..., R. Dimova. 2018. Charged giant unilamellar vesicles prepared by electroformation exhibit nanotubes and transbilayer lipid asymmetry. *Sci. Rep.* 8:11838.
45. Weinberger, A., F. C. Tsai, ..., C. Marques. 2013. Gel-assisted formation of giant unilamellar vesicles. *Biophys. J.* 105:154–164.
46. Riske, K. A., and R. Dimova. 2005. Electro-deformation and poration of giant vesicles viewed with high temporal resolution. *Biophys. J.* 88:1143–1155.
47. Agudo-Canalejo, J., and R. Lipowsky. 2015. Critical particle sizes for the engulfment of nanoparticles by membranes and vesicles with bilayer asymmetry. *ACS Nano*. 9:3704–3720.
48. Robinson, T., P. Kuhn, ..., P. S. Dittrich. 2013. Microfluidic trapping of giant unilamellar vesicles to study transport through a membrane pore. *Biomicrofluidics*. 7:44105.
49. Robinson, T., P. E. Verboket, ..., P. S. Dittrich. 2014. Controllable electrofusion of lipid vesicles: initiation and analysis of reactions within biomimetic containers. *Lab Chip*. 14:2852–2859.
50. Skelley, A. M., O. Kirak, ..., J. Voldman. 2009. Microfluidic control of cell pairing and fusion. *Nat. Methods*. 6:147–152.
51. Yoon, T. Y., B. Okumus, ..., T. Ha. 2006. Multiple intermediates in SNARE-induced membrane fusion. *Proc. Natl. Acad. Sci. USA*. 103:19731–19736.
52. Mattei, B., R. B. Lira, ..., K. A. Riske. 2017. Membrane permeabilization induced by Triton X-100: the role of membrane phase state and edge tension. *Chem. Phys. Lipids*. 202:28–37.
53. Aranda, S., K. A. Riske, ..., R. Dimova. 2008. Morphological transitions of vesicles induced by alternating electric fields. *Biophys. J.* 95:L19–L21.
54. Dimova, R., K. A. Riske, ..., R. Lipowsky. 2007. Giant vesicles in electric fields. *Soft Matter*. 3:817–827.
55. Riske, K. A., T. P. Sudbrack, ..., R. Itri. 2009. Giant vesicles under oxidative stress induced by a membrane-anchored photosensitizer. *Biophys. J.* 97:1362–1370.
56. Mattei, B., A. D. França, and K. A. Riske. 2015. Solubilization of binary lipid mixtures by the detergent Triton X-100: the role of cholesterol. *Langmuir*. 31:378–386.
57. Dimova, R., N. Bezlyepkina, ..., R. Lipowsky. 2009. Vesicles in electric fields: some novel aspects of membrane behavior. *Soft Matter*. 5:3201–3212.
58. Wong, J. L., D. E. Koppel, ..., G. M. Wessel. 2007. Membrane hemifusion is a stable intermediate of exocytosis. *Dev. Cell*. 12:653–659.
59. White, J. M., and J. D. Castle. 2005. Searching for the silver lining. *Nat. Struct. Mol. Biol.* 12:382–384.
60. McIntyre, J. C., and R. G. Sleight. 1991. Fluorescence assay for phospholipid membrane asymmetry. *Biochemistry*. 30:11819–11827.
61. Moreno, M. J., L. M. Estronca, and W. L. Vaz. 2006. Translocation of phospholipids and dithionite permeability in liquid-ordered and liquid-disordered membranes. *Biophys. J.* 91:873–881.
62. Bezlyepkina, N., R. S. Gracià, ..., R. Dimova. 2013. Phase diagram and tie-line determination for the ternary mixture DOPC/eSM/cholesterol. *Biophys. J.* 104:1456–1464.
63. Stamatatos, L., R. Leventis, ..., J. R. Silvius. 1988. Interactions of cationic lipid vesicles with negatively charged phospholipid vesicles and biological membranes. *Biochemistry*. 27:3917–3925.
64. Islam, M. Z., H. Ariyama, ..., M. Yamazaki. 2014. Entry of cell-penetrating peptide transportan 10 into a single vesicle by translocating across lipid membrane and its induced pores. *Biochemistry*. 53:386–396.
65. Biner, O., T. Schick, ..., C. von Ballmoos. 2016. Delivery of membrane proteins into small and giant unilamellar vesicles by charge-mediated fusion. *FEBS Lett.* 590:2051–2062.
66. Lakowicz, J. R. 2006. Principles of Fluorescence Spectroscopy. Springer, New York.
67. Li, Y., R. Lipowsky, and R. Dimova. 2011. Membrane nanotubes induced by aqueous phase separation and stabilized by spontaneous curvature. *Proc. Natl. Acad. Sci. USA*. 108:4731–4736.

68. Bassereau, P., R. Jin, ..., T. R. Weikel. 2018. The 2018 biomembrane curvature and remodeling roadmap. *J. Phys. D Appl. Phys.* 51:343001.
69. Lipowsky, R. 2013. Spontaneous tubulation of membranes and vesicles reveals membrane tension generated by spontaneous curvature. *Faraday Discuss.* 161:305–331, discussion 419–459.
70. Dasgupta, R., M. S. Miettinen, ..., R. Dimova. 2018. The glycolipid GM1 reshapes asymmetric biomembranes and giant vesicles by curvature generation. *Proc. Natl. Acad. Sci. USA.* 115:5756–5761.
71. Solon, J., J. Pécéréaux, ..., P. Bassereau. 2006. Negative tension induced by lipid uptake. *Phys. Rev. Lett.* 97:098103.
72. Georgiev, V. N., A. Grafmüller, ..., R. Dimova. 2018. Area increase and budding in giant vesicles triggered by light: behind the scene. *Adv. Sci. (Weinh.)* 5:1800432.
73. Mertins, O., and R. Dimova. 2013. Insights on the interactions of chitosan with phospholipid vesicles. Part II: membrane stiffening and pore formation. *Langmuir* 29:14552–14559.
74. Fricke, N., and R. Dimova. 2016. GM1 softens POPC membranes and induces the formation of micron-sized domains. *Biophys. J.* 111:1935–1945.
75. Bhatia, T., J. Agudo-Canalejo, ..., R. Lipowsky. 2018. Membrane nanotubes increase the robustness of giant vesicles. *ACS Nano* 12:4478–4485.
76. Weber, T., B. V. Zemelman, ..., J. E. Rothman. 1998. SNAREpins: minimal machinery for membrane fusion. *Cell* 92:759–772.
77. Kyoung, M., A. Srivastava, ..., A. T. Brunger. 2011. In vitro system capable of differentiating fast Ca<sup>2+</sup>-triggered content mixing from lipid exchange for mechanistic studies of neurotransmitter release. *Proc. Natl. Acad. Sci. USA.* 108:E304–E313.
78. Nickel, W., T. Weber, ..., J. E. Rothman. 1999. Content mixing and membrane integrity during membrane fusion driven by pairing of isolated v-SNAREs and t-SNAREs. *Proc. Natl. Acad. Sci. USA.* 96:12571–12576.
79. Starai, V. J., Y. Jun, and W. Wickner. 2007. Excess vacuolar SNAREs drive lysis and Rab bypass fusion. *Proc. Natl. Acad. Sci. USA.* 104:13551–13558.
80. Engel, A., and P. Walter. 2008. Membrane lysis during biological membrane fusion: collateral damage by misregulated fusion machines. *J. Cell Biol.* 183:181–186.
81. Smith, E. A., and J. C. Weisshaar. 2011. Docking, not fusion, as the rate-limiting step in a SNARE-driven vesicle fusion assay. *Biophys. J.* 100:2141–2150.
82. van Lengerich, B., R. J. Rawle, ..., S. G. Boxer. 2013. Individual vesicle fusion events mediated by lipid-anchored DNA. *Biophys. J.* 105:409–419.
83. Simonsson, L., P. Jönsson, ..., F. Höök. 2010. Site-specific DNA-controlled fusion of single lipid vesicles to supported lipid bilayers. *Chemphyschem* 11:1011–1017.
84. Rawle, R. J., B. van Lengerich, ..., S. G. Boxer. 2011. Vesicle fusion observed by content transfer across a tethered lipid bilayer. *Biophys. J.* 101:L37–L39.
85. Yu, M., R. B. Lira, ..., H. Lin. 2015. Ellipsoidal relaxation of deformed vesicles. *Phys. Rev. Lett.* 115:128303.
86. Shillcock, J. C., and R. Lipowsky. 2005. Tension-induced fusion of bilayer membranes and vesicles. *Nat. Mater.* 4:225–228.
87. Kozlov, M. M., and L. V. Chernomordik. 2015. Membrane tension and membrane fusion. *Curr. Opin. Struct. Biol.* 33:61–67.
88. Koltover, I., T. Salditt, ..., C. R. Safinya. 1998. An inverted hexagonal phase of cationic liposome-DNA complexes related to DNA release and delivery. *Science* 281:78–81.
89. Lin, A. J., N. L. Slack, ..., C. R. Safinya. 2003. Three-dimensional imaging of lipid gene-carriers: membrane charge density controls universal transfection behavior in lamellar cationic liposome-DNA complexes. *Biophys. J.* 84:3307–3316.
90. Ewert, K. K., A. Ahmad, ..., C. R. Safinya. 2005. Cationic lipid-DNA complexes for non-viral gene therapy: relating supramolecular structures to cellular pathways. *Expert Opin. Biol. Ther.* 5:33–53.



**Biophysical Journal, Volume 116**

**Supplemental Information**

**Highly Efficient Protein-free Membrane Fusion: A Giant Vesicle Study**

**Rafael B. Lira, Tom Robinson, Rumiana Dimova, and Karin A. Riske**

## S1. Materials and methods

**S1.1 Materials.** The phospholipids 1-palmitoyl-2-oleoyl-sn-glycero-3-phosphocholine (POPC), 1-palmitoyl-2-oleoyl-sn-glycero-3-phospho-(1'-rac-glycerol), sodium salt (POPG), 1,2-dioleoyl-sn-glycero-3-phosphoethanolamine (DOPE), 1,2-dioleoyl-3-trimethylammonium-propane (DOTAP), the fluorescent dyes 1,2-dipalmitoyl-sn-glycero-3-phosphoethanolamine-N-(lissamine rhodamine B sulfonyl) (ammonium salt) (DPPE-Rh) and 1-oleoyl-2-{6-[(7-nitro-2-1,3-benzoxadiazol-4-yl)amino]hexanoyl}-sn-glycero-3-phosphoethanolamine (DPPE-NBD) were purchased from Avanti Polar Lipids (Alabaster, AL). Atto 647 was from Atto-Tec (Siegen, Germany). Lipid solutions were prepared in chloroform and stored at -20°C until use. Sulforhodamine B (SRB), sodium chloride (NaCl), calcium chloride (CaCl<sub>2</sub>), sucrose, glucose and sodium dithionite were purchased from Sigma Aldrich (St. Louis, MO) and used as received. Low-melting temperature agarose was purchased from Fisher scientific (Waltham, MA).

**S1.2 Vesicle preparation and incubation.** Giant unilamellar vesicles (GUVs) were produced by the electroformation method (1) as described in detail in Ref. (2). Briefly, a 6-8 µl lipid solution of a given lipid mixture (3 mM) in chloroform was spread on conductive indium tin oxide glass plates and the solvent was evaporated for ~ 5 minutes under a stream of N<sub>2</sub>. Additional vacuum has no influence on the results or on the mechanical properties (3). A 1 mm Teflon spacer was sandwiched between the glass plates forming a chamber of ~ 2 mL volume, that was connected to a function generator (1.6 Vpp nominal voltage at 10 Hz) and a 200 mM sucrose solution was added. Vesicles were allowed to grow at room temperature for 1-2 hours. Alternatively, GUVs containing 100 mol% POPG were also produced by the PVA-lipid method to improve vesicle yield exactly as described in Ref. (3). When fluorescent dyes were used, growth was performed in the dark. DPPE-Rh was used at 0.1 mol% for observation and 0.5 mol% for FRAP, whereas DPPE-NBD was used at 0.5-1 mol%.

Large unilamellar vesicles (LUVs) with fusogenic properties were produced by the film hydration method followed by extrusion. Briefly, an aliquot of DOPE:DOTAP:DPPE-Rh was mixed at 1:1:0.1 mol ratio in chloroform at a given concentration. Alternatively, DPPE-NBD was used instead of DPPE-Rh at the same molar fraction. The solution was deposited on the bottom of a glass vial and dried under a stream of N<sub>2</sub>. The lipid film was further dried in a vacuum for at least two hours and then hydrated with a 0.2 M sucrose solution to yield a 2.1 mM final lipid concentration. The solution was vortexed until complete lipid detachment from the glass. The formed multilamellar vesicles were extruded with a mini-extruder (Avanti Polar Lipid – Alabaster, AL) through a 100 nm pore diameter polycarbonate membrane 11 times for LUV formation. LUVs were usually used fresh but alternatively stored at 4°C and used within 4 days. Routine zeta potential and dynamic light scattering (DLS) measurements showed that the vesicles are stable for at least a month and they are still fusogenic, but these vesicles were never used for measurements. The zeta potential and DLS measurements were performed on ZetaSizer Nano ZS (Malvern, UK) instrument operating with a 4 mW HeNe laser (632.8 nm) and a detector positioned at the scattering angle of 173°.

The GUVs were placed in a chamber made of two coverslips separated by a 2 mm thick ring made of Teflon (observation chamber), diluted in ~ 5X in isoosmolar glucose and observed under the microscope. Incubation was typically carried out directly on the chamber, either by adding GUVs to a homogeneous LUV suspension, or by adding a concentrated LUV solution to GUVs sitting at the bottom of the chamber (final 30 µM concentration of LUV lipids in both cases). Alternatively, LUV-GUV incubation was carried out in an Eppendorf tube. For NBD quenching experiments to probe membrane hemifusion versus full-fusion, non-labeled POPC GUVs were incubated with 1 µM NBD-labeled LUVs for ten minutes. Incubation was done in the presence of 5 µM SRB to detect GUV leakage. A fraction of this sample was then incubated with 10 mM sodium dithionite for another ten minutes and then used for

observation. For three-dimensional GUV imaging and for FRAP (see below), the samples were incubated for 10 minutes and then mixed with a fluid agarose solution (0.1-0.5% w/v final agarose concentration) for GUV immobilization. This mixture was allowed to cool down at room temperature for at least 10 minutes for subsequent imaging. This step immobilized the GUVs and facilitated performing the measurements (4). At this agarose concentration, LUVs are not fully immobilized.

**S1.3 Microscopy.** Phase-contrast microscopy was performed in a Zeiss Axiovert 200 (Jena, Germany) or with a Zeiss Axio Observer.D1 microscope using a 20X air (0.5 NA) or a 40X (0.6 NA) objectives. Both microscopes were equipped with a digital camera PCO.edge 4.2 (Kelheim, Germany). For electrodeformation experiments, 100  $\mu$ l of the GUV solution was placed in an electrofusion chamber (Eppendorf, Germany) with parallel cylindrical electrodes (92  $\mu$ m radius) spaced at 500  $\mu$ m. The chamber was connected to a function generator and the AC field (100 V/cm and 100 Hz frequency) was turned on. In one corner of the chamber, 20  $\mu$ l of a 0.2 mM LUVs (lipid concentration) was added and reached the GUVs by diffusion. The final chamber volume was 1 ml. Only initially spherical GUVs were chosen for analysis. ImageJ (NIH, USA) was used for general image analysis and measurements.

Confocal microscopy was performed on a Leica TCS SP5 (Wetzlar, Germany) confocal microscope using 40X (0.75 NA) air or 63X (1.2 NA) water immersion objectives. DPPE-NBD was excited with an argon laser at 488 nm and SRB and DPPE-Rh were excited with a diode-pumped solid-state laser at 561 nm. The emission signals were collected at 490-545 nm and 565-650 nm, respectively. Spatial and temporal resolutions were adjusted according to the measurements, but typically 512x512 pixels, at 400 Hz (bidirectional scanning) with a 1 Airy unit pinhole were selected. The same settings were used for imaging GUVs with different Rh/NBD ratios for construction of a FRET calibration curve and later its ratio upon LUV-GUV fusion to measure FRET efficiency (see results in the main text).

## S2. Lipid transfer to neutral and negative GUVs

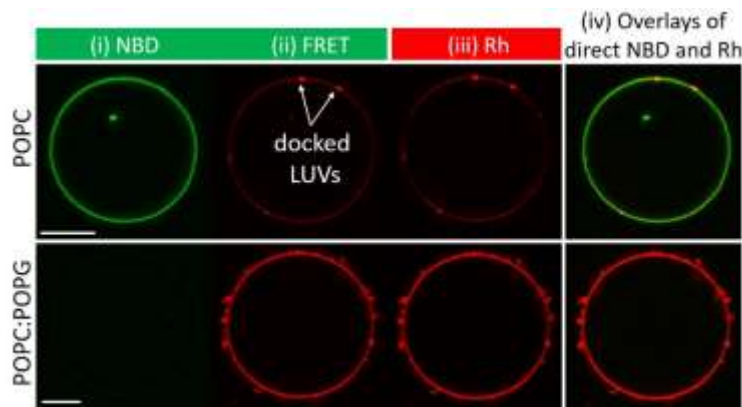


**Figure S1.** Lipid transfer from DPPE-Rh-containing LUVs to neutral (POPC) and negative (POPC:POPG, 1:1) GUVs containing DPPE-NBD: panels (i) and (iii) show signal after direct excitation and emission of NBD and Rh, respectively, (ii) shows FRET signal from NBD excitation and detection of Rh fluorescence; (iv) merged images of NBD and Rh direct excitation and emission channels, (i) and (iii) respectively. LUVs docked on the surface of GUVs can be observed both through direct Rh excitation and emission (iii) as well as via FRET (ii), provided LUV lipids are transferred to GUVs. On the contrary, they are not observed upon NBD direct excitation and emission (i). Charged GUVs cannot be observed in the NBD channel because of the high FRET efficiency resulting from fusion. Images were identically contrast-enhanced for better visualization. Scale bars: 10  $\mu$ m.



### S3. Number of stably docked LUVs on neutral and negative GUVs

LUVs were added to suspensions of neutral or negative GUVs settled on the bottom of the observation chamber. After 10 minutes incubation, the samples were immobilized in agarose following the protocol developed in Ref. (4). The number of stably docked LUVs (i.e. LUVs which do not detach after the incubation) was measured by counting the number of diffraction-limited red spots (i.e. LUVs) on every x-y cross-section from a z-stack for 3D reconstruction upon direct rhodamine excitation (the numbers may be an underestimate if multiple LUVs are counted as one). Because of their size and fluorescence intensity, membrane buds/folds are usually easily discernible from docked LUVs, the latter being less fluorescent. The results are shown in Figure S2. To correct for the size difference of the GUVs, the data are presented as density of docked LUVs,  $n_{\text{LUVs}}/\mu\text{m}^2$ , onto the GUV surface area. The data for neutral POPC GUVs are largely scattered, which might be a result of non-homogeneous mixing of LUVs and GUVs. The value of  $n_{\text{LUVs}}$  for negative POPC:POPG (1:1, mol ratio) is significantly lower (and less scattered). Note that the majority of docked LUVs have proceeded to full fusion and are not counted as stably docked LUVs.

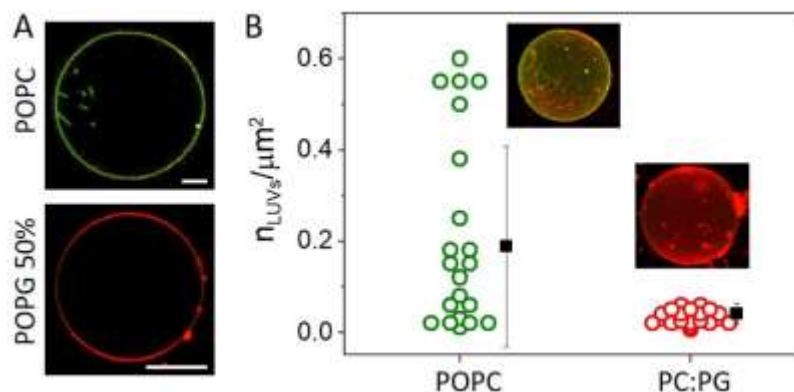


**Figure S2.** Measuring the number of docked LUVs  $n_{\text{LUVs}}$  on GUVs. (A) Example equatorial section overlays of a neutral (POPC) and a negative (POPC:POPG, 1:1 mol) GUV. Scale bars: 10  $\mu\text{m}$ . (B) Number of stably docked LUVs,  $n_{\text{LUVs}}$ , per 1  $\mu\text{m}^2$  GUV area shown for neutral and negative GUVs. Each point represents a measurement on a single GUV. Mean averages and standard error are also shown (black). Inset: 3D reconstructions of the vesicles shown in (A).

### S4. Probing fusion in real-time in a microfluidic device

**S4.1 Microfluidic chip fabrication.** The design of the microfluidic device and its fabrication are described in detail elsewhere (5, 6). A lower PDMS layer contained micro-channels for the vesicle solutions as well as the micro-posts for capturing the GUVs. A second upper PDMS layer contains micro-channels with circular designs that can be hydraulically pressurized to actuate ring-valves in the lower channels. Briefly, a 10:1 ratio of PDMS oligomer and curing agent (Sylgard 184, Dow Corning) was poured over a silicon wafer master for the upper layer (with feature heights at 20  $\mu\text{m}$ ) to a final thickness of 5 mm. The same mixture was spin coated onto a second silicon wafer for the lower layer (feature heights also at 20  $\mu\text{m}$ ) at 2000 rpm to a height of 40  $\mu\text{m}$ . Both were then cured at 80  $^{\circ}\text{C}$  for 3 h. After removal of the upper layer

from the master, 1 mm holes were punched (Biopsy puncher, Miltex) for the hydraulic pressure. After exposing the upper and lower layers to an air plasma for 60 s at 0.5 mbar (PDC-002, Harrick Plasma), the two were aligned under a microscope by hand and placed in an oven for 2 h at 80 °C to complete the bonding process. The assembly was removed from the lower layer master and 1.5 mm fluidic access holes were punched (Biopsy puncher, Miltex). Finally, this was bonded to a 0.17 mm glass coverslip with the same air plasma and left for 30 min at 60 °C.

**S4.2 Operation of microfluidic device.** The fluidic and pressure control channels were pre-filled with 0.2 M glucose hosting solution by centrifugation for 10 min at an RCF of 900. This guarantees a bubble-free environment within the channel network. GUV and LUV suspensions were introduced into the device via a reservoir attached to the top of the PDMS device and drawn into the micro-channels using PTFE tubing (O.D. = 1/16" and I.D. = 0.8 μm), a glass syringe (1 mL, Agilent), and a syringe pump (low pressure module, neMESYS) operating in reverse mode. Flow rates were between 2 - 10 μL/min. The ring-valves surrounding each trap were actuated by pressurizing the upper control layer with 0 or 3 bar of air to instantaneously open or close them respectively.

**S4.3 Probing fusion in a microfluidic chamber.** Controlled fusion of LUVs and GUVs was probed in a microfluidic chamber. Microfluidic experiments allow rapid exchange of solution and reactants by opening and closing the valves. In the setup here, physical posts are used as traps to immobilize GUVs under flow. The fluidic exchange times were then determined for various flow rates. As shown in Figure S3B, the chamber was filled with a 10 μM calcein solution (upper image). A confocal time series were acquired as the valve was opened and the dye was replaced with pure water (lower image) for flow rates of 0.5 to 10 μL/min. At a flow rate of 2 μL/min, the calcein solution is completely exchanged in 400 ms (Figure S3B). The fluid exchanging time depends on flow rate but is constant (~ 400 ms) at flow rates higher than 2 μL/min. The two non-fluorescent spots in the image are the PDMS posts used for GUV immobilization as schematically illustrated in Figure S3A. The approach consists of immobilizing a single GUV at the posts followed by subsequent addition of the fusogenic LUVs.

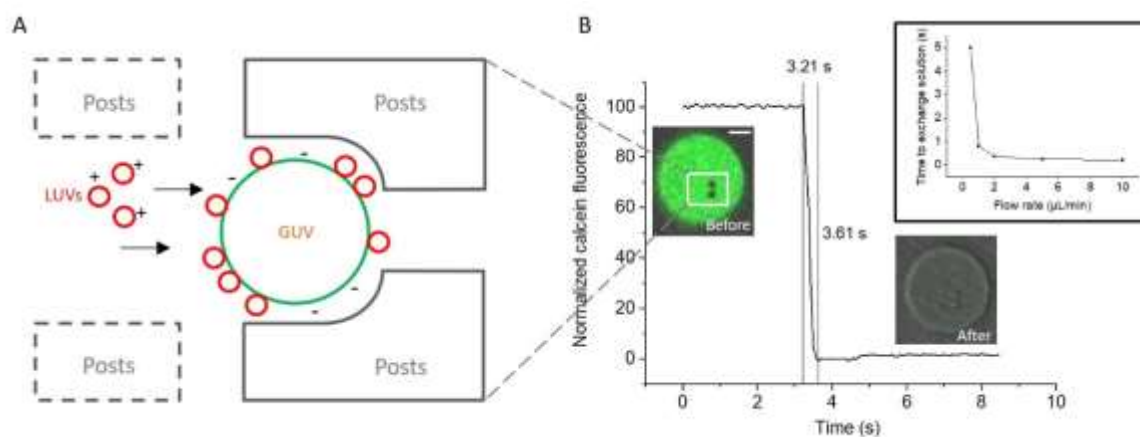


**Figure S3.** Microfluidic solution exchange and GUV immobilization. (A) The PDMS posts are schematically shown for GUV immobilization and subsequent LUV addition. Additional posts (dashed) were used for fusion experiments. (B) Exchange of calcein solution (10 μM) at 2 μL/min. Inset images: Overlays of confocal and bright-field images before and after flushing the calcein away with a calcein-free solution. The fluorescent circular area in the upper inset shows the microfluidic chamber (created by a ring-valve) for GUV trapping and controlled solution exchange (the two black spots inside are the PDMS posts). Scale bar: 50 μm. Inset figure: fluidic exchange times were then determined for various flow rates.

Fusion efficiency was probed by first immobilizing a negative GUV (loaded at 10  $\mu\text{L}/\text{min}$  until > 90% of traps are occupied) and then adding the LUVs at a flow rate of 2  $\mu\text{L}/\text{min}$ . This flow rate was chosen for fast fluid exchange (delivery of LUVs) without losing GUVs due to excess hydrodynamic forces. The changes in donor (NBD) and acceptor (Rh) fluorescence were measured upon donor excitation (FRET channel). As shown in Figure S4, addition of LUVs results in NBD fluorescence intensity decrease along with an increase in fluorescence in the FRET channel. Rh fluorescence changes upon direct Rh excitation are also shown. The onset of LUV addition is  $t = 0$ .

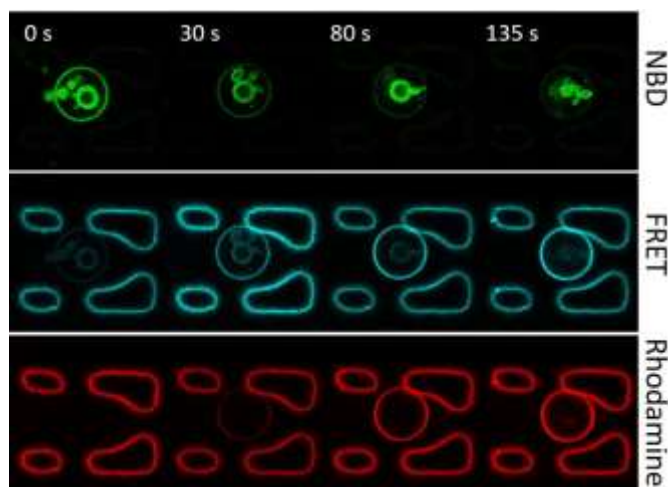


**Figure S4.** Mixing of LUVs and GUVs in a microfluidic chamber. Confocal cross sections of a negative GUV trapped in the PDMS posts (same as in Figure 3A in the main text and in Movie S1) upon NBD direct excitation (green), NBD excitation and Rh detection, i.e. FRET (turquoise) and direct Rh excitation (red). LUVs (30  $\mu\text{M}$  lipids) are added at  $t = 0$  s at a flow rate of 2  $\mu\text{L}/\text{min}$ . Membranous structures inside the GUV remain inaccessible to the LUVs (compare green and red channels).

## S5. Intensity-based FRET

**S5.1 Intensity-based FRET as a lipid mixing assay.** GUVs (30  $\mu\text{L}$ ) containing 0.5 mol% DPPE-NBD (head-group labeled) and DPPE-Rh-containing LUVs (30  $\mu\text{M}$  lipid concentration) were mixed in an Eppendorf tube to 130  $\mu\text{L}$  total solution in 200 mM glucose. The GUVs were incubated for 10 minutes. An aliquot was then transferred to a chamber for microscopy observation.

We selected three different imaging channels; (i) the direct donor (DPPE-NBD) excitation and detection, (ii) donor excitation and acceptor (DPPE-Rh) detection, and (iii) direct acceptor excitation and detection. Imaging was performed in the sequential mode to minimize cross-talk. For FRET signal calculation, the first two channels were used, whereas the third was important for detecting the interacting LUVs. The relative FRET efficiency ( $E_{FRET}$ ) was measured according  $E_{FRET} = I_{Rh} / (I_{Rh} + I_{NBD})$  where  $I_{Rh}$  and  $I_{NBD}$  are the respective rhodamine and NBD fluorescence intensities when only NBD is excited(7). Intensities were measured from the integrated area of a profile across the GUVs. The line crosses the vertical segment of the vesicle where intensity is highest (due to fluorescence polarization of Rh the membrane). This approach was chosen to avoid unwanted signals from docked LUVs.

**S5.2 Intensity FRET-based assay to determine membrane composition upon fusion.** In order to quantify fusion efficiency and to determine GUV composition after fusion with LUVs from the changes in fluorescence, we constructed a calibration curve mimicking possible acceptor-donor ratios observed after fusion. POPC GUVs containing a fixed concentration of DPPE-NBD (0.5 mol%, as in the fusion experiments) were prepared with increasing mole fractions of DPPE-Rh. Their FRET efficiency  $E_{FRET} = I_{Rh}/(I_{Rh} + I_{NBD})$  was measured for the increasing donor/acceptor ratios (Rh/NBD). As DPPE-Rh concentration was increased, the Rh emission fluorescence (defined as the acceptor fluorescence upon donor excitation) also increased, along with a decrease in donor (NBD) fluorescence. This is illustrated in Figure S5A. Above the images we indicated the changes in Rh/NBD ratio for increasing DPPE-Rh molar fraction, and below them we give the experimentally measured  $E_{FRET}$ . Figure S5B summarizes the measured  $E_{FRET}$  values of the different Rh/NBD ratios tested across all GUVs. The maximum and minimum Rh concentrations were chosen by observing the Rh intensities during a fusion experiment using identical confocal microscope settings. Note that the sensitivity of the assay decreases as  $E_{FRET}$  approaches 1 (schematically indicated with the gray area in Figure S5B). From the calibration curve and the images of fused GUVs, it is possible to deduce the molar ratio of Rh/NBD from measurements of  $E_{FRET}$  on the level of single GUVs, and translate it to changes in membrane compositions.

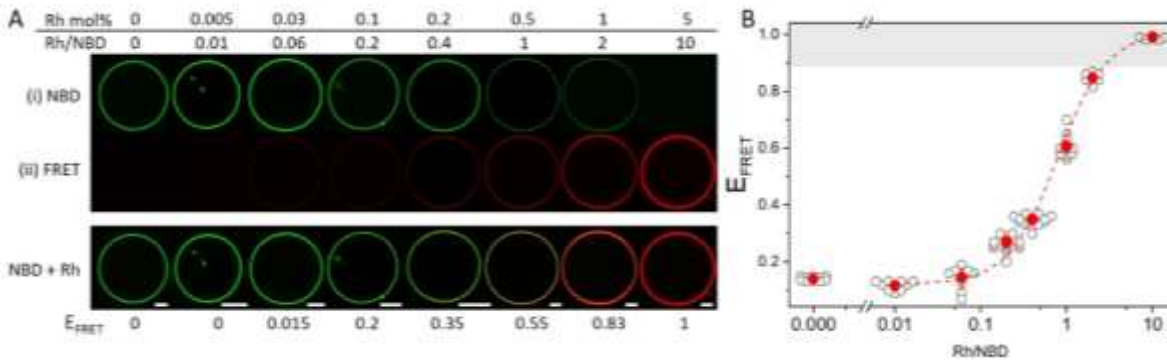


**Figure S5.** Construction of a FRET calibration curve for deducing the composition of GUVs after fusion. (A) GUV images as detected from (i) NBD and (ii) Rh fluorescence upon NBD excitation. The membrane composition is a fixed amount of DPPE-NBD (0.5 mol%) with increasing DPPE-Rh mole fractions as indicated above. The microscopy settings for each of the different vesicles were identical. Due to FRET, Rh fluorescence increases at the expense of NBD fluorescence. (iii) Overlay of DPPE-NBD and DPPE-Rh direct excitation. The  $E_{FRET}$  values for the particular GUVs are shown below the images. Scale bars: 10  $\mu\text{m}$ . (B) Calibration curve of measured  $E_{FRET}$  values as a function of Rh/NBD ratio. Each data point corresponds to one measurement on a single GUV (grey circles). Mean average and standard deviations are also shown (red). The curve is a guide to the eye. The grey area corresponds to the limited FRET sensitivity region in which  $E_{FRET}$  approaches 1 by definition.

From the  $E_{FRET}$  value measured on the fused GUV and the corresponding Rh/NBD ratio,  $r_{Rh/NBD}$ , which would produce such FRET signal as deduced from the calibration curve in Figure S5, one can calculate the molar fraction of DOTAP transferred from the LUVs to the GUVs

$$DOTAP\% = \frac{5r_{Rh/NBD}}{100 + 10.5r_{Rh/NBD}} \quad (S1)$$



## S6. LUV-induced adhesion and rupture of neutral GUVs

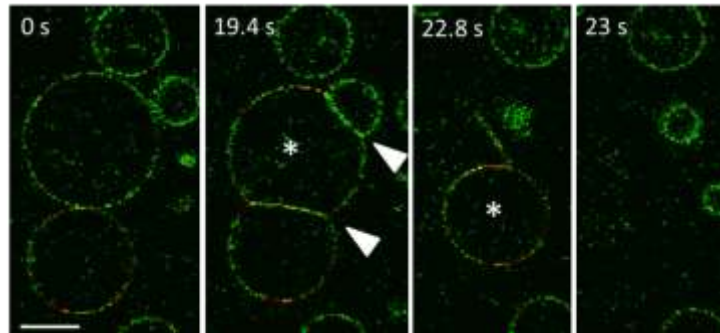


**Figure S6.** LUV-mediated adhesion of neutral GUVs followed by rupture. LUVs are added in one corner of the chamber (to 30  $\mu\text{M}$  final lipid concentration) and reach the POPC GUVs by diffusion. LUVs induce GUV-GUV adhesion (arrows) and increase the membrane tension of the GUVs which eventually rupture. Two rupture events are shown (asterisks indicates the GUV that ruptures on the next frame). Scale bar: 20  $\mu\text{m}$ .

## S7. Quenching of DPPE-NBD lipids on the external GUV leaflet by dithionite

**S7.1 Quenching of POPC vesicles with both leaflets labeled with NBD.** To selectively quench NBD lipids in the outer leaflet of GUVs, POPC GUVs containing 1 mol% DPPE-NBD were incubated in an Eppendorf tube with 10 mM of the quencher dithionite and then observed under epifluorescence or confocal microscopy. For quenching experiments, it is also important to check for changes in membrane integrity to ensure dithionite does not leak in and quench the inner monolayer NBD as well. For that, epifluorescence or confocal microscopy was used along with phase contrast images to detect sucrose/glucose leakage. Figure S7 shows confocal (left) and phase contrast images (right) of POPC GUVs in the absence (upper) and presence of dithionite (middle). There is a significant reduction in DPPE-NBD fluorescence upon incubation with dithionite. The lower panel in Figure S7A shows a GUV that became permeable and lost its contrast. Note that NBD fluorescence decreases to almost background value when the vesicle becomes permeable because it allows quenching of the dye in both the outer and inner leaflets. For the quenching analysis we excluded vesicles which have leaked, which at this concentration of dithionite represented a fraction of 5% or less. Figure S7B shows the maximum intensity along a line shown in panel A in the absence (green) and presence (black) of dithionite for intact GUVs. The membrane intensity was assessed from the peak maxima (at the position of the membrane) from the line profiles. Figure S7C shows measurements on 12-13 GUVs. In the presence of dithionite, NBD fluorescence of non-permeable GUVs decreases by  $\sim 50\%$ , demonstrating the selective quenching of outer leaflet NBD.

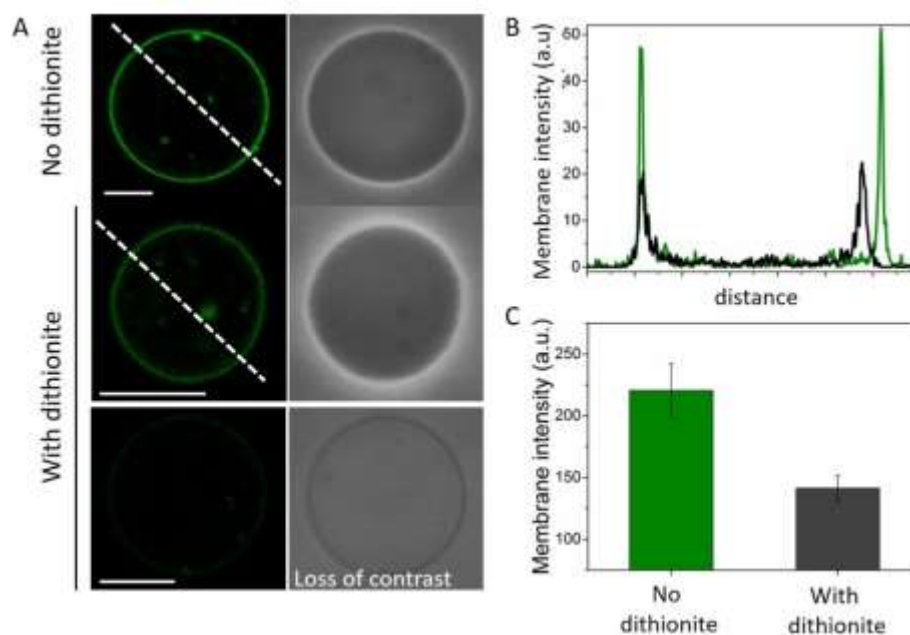


**Figure S7.** NBD quenching by dithionite in vesicles made of POPC and 1 mol% DPPE-NBD. (A) Confocal (left) and phase contrast (right) images of GUVs in the absence (upper panel) and presence of 10 mM dithionite (middle and lower panel). Scale bars: 10  $\mu$ m. In B, NBD fluorescence intensity along the lines shown in A. In C, measurements performed using epifluorescence microscopy for GUVs in the absence (green) and presence of dithionite (black).

**S7.2 Quenching of POPC vesicles with only outer leaflet labeled with NBD.** To mimic GUVs that have undergone hemifusion, we used GUVs containing DPPE-NBD exclusively in the external leaflet. To prepare such asymmetric vesicles, 20  $\mu$ L of non-labeled POPC GUVs were incubated for 20 min with 2  $\mu$ L of free DPPE-NBD (0.29 mM in ethanol). The vesicles were then harvested and dispersed in isoosmolar glucose to 100  $\mu$ L final volume. The incubation with DPPE-NBD makes the GUV membrane fluorescent, see images in Figure S8. We measured the membrane intensity (maximum peak intensity from line profiles across the vesicle) in non-labeled GUVs, vesicles incubated with DPPE-NBD, and vesicles incubated with DPPE-NBD and later with 10 mM dithionite. When vesicles with labeled outer leaflet are incubated with dithionite, their fluorescence is almost completely quenched since the dye and the quencher were located in the same side of the membrane. This demonstrates that the assay is functional and can distinguish hemifusion and full fusion from complete and partial quenching of NBD, respectively.

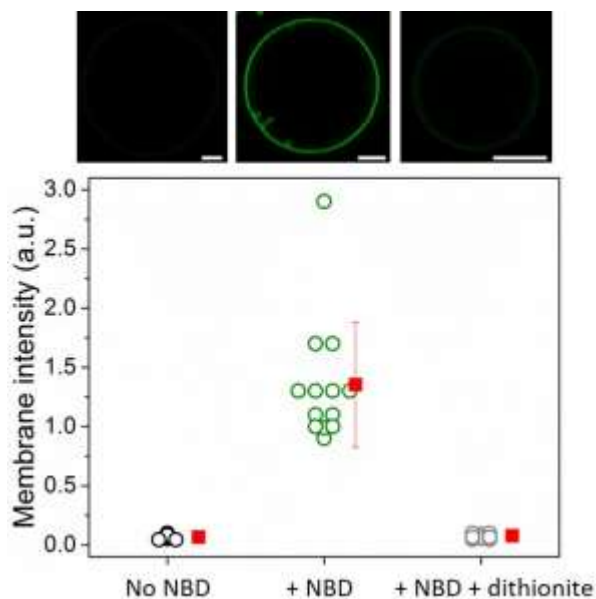


**Figure S8.** Quenching of asymmetrically labeled GUVs: confocal cross sections and intensity data from non-labeled POPC GUVs in the absence of DPPE-NBD, incubated with DPPE-NBD, and incubated with DPPE-NBD and dithionite. Scale bars: 10  $\mu\text{m}$ .

**S7.3 Incubation of neutral and negative GUVs with dithionite.** Sodium dithionite was used to probe LUV hemifusion or full fusion with GUVs. Whereas the experiments could be readily performed with neutral GUVs, negative vesicles displayed a very strong propensity to become damaged in the presence of 10 mM dithionite. They typically collapsed, forming multiple bilayers due to membrane aggregation and the resulting smaller vesicles were permeable (see Figure S9). This behavior was observed even at 1 mM dithionite, a concentration at which neutral GUVs are not fully quenched. Therefore, it was not possible to use the dithionite assay to quench NBD in order to probe hemifusion or full fusion using highly charged GUVs.

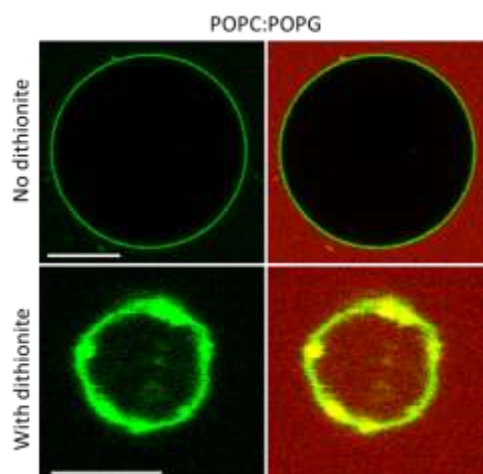


**Figure S9.** Damage of negative (POPC:POPG 1:1) GUVs in the presence of sodium dithionite. The upper row shows a negative, initially non-labeled GUV, incubated with 1  $\mu$ M NBD-labeled LUVs and in the absence of dithionite. The vesicle is not permeable to SRB (red signal on the right). The lower panel shows that negative GUVs are strongly damaged in the presence of 10 mM dithionite. Scale bar: 10  $\mu$ m.

**S7.4 Effect of dithionite on the permeability of fusogenic LUVs.** The fluorescence of the NBD-labeled LUVs was completely quenched in the presence of dithionite, which suggests that this agent is able to easily permeate across the membrane of the fusogenic LUVs. In order to probe possible membrane permeation induced by sodium dithionite, we prepared DPPE-Rh-labeled fusogenic LUVs in the presence of 20  $\mu$ M Atto647, a water-soluble dye. The LUV dispersion was prepared in a high lipid concentration (2 mM) and diluted to 30  $\mu$ M so that most of the Atto647 was encapsulated. The membrane dye Rh was chosen due to its insensitivity to quenching by dithionite. Figure S10 A shows 6 LUVs dispersed in isotonic glucose as a control. Note that almost all vesicles (identified as red dots) preserve their content (white dots). Figure S10 B shows the fluorescence intensities in the membrane (top) and content (bottom) channels. Instances of content loss are observed by a red dot lacking its content signal, as indicated by the arrows, but such events were rare in control conditions. As a positive control, we dispersed the vesicles in 1 mM Triton X-100 to induce complete solubilization of LUVs. No red spots were detected and Atto647 was therefore completely released (not shown). In the presence of 10 mM sodium dithionite, more vesicles were observed to be empty, whereas most of the remaining vesicles displayed a significant reduction in their content signal, as observed in Figure S10 C and D. Because of its smaller size (174 Da) compared to Atto647 (593 Da), we believe that sodium dithionite may permeate even more. We thus conclude that the NBD-labeled LUVs used in the main text are permeable to sodium dithionite, fully quenching their fluorescence regardless of the presence of GUVs. However, we must point out that our conclusions of membrane hemi- or full-fusion still hold, considering that sodium dithionite was added only after LUV-GUV fusion has occurred, and that the measurements on GUVs were performed exclusively on vesicles that were impermeable to rule out any effects of dithionite leakage into the GUVs.



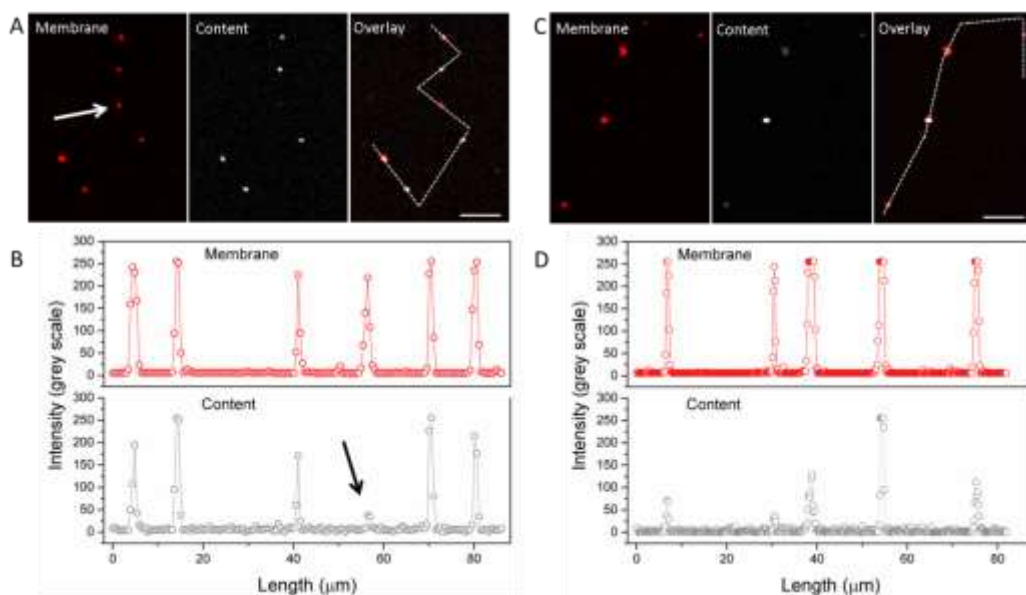


**Figure S10.** Small LUVs (DOTAP:DOPE:Rh-PE, 1:1:0.1 mol) encapsulating 20 μM Atto647 prepared in sucrose 200 mM and dispersed in isoosmolar glucose with (C, D) and without (A, B) 10 mM dithionite. Panels A and C show the DPPE-Rh (red; membrane), Atto647 (white; content) and overlay channels. Panels B and D show the fluorescence intensity for both channels along the path shown in the overlay images. The arrow indicates one LUV devoid of Atto647. Bars: 10 μm.

## S8. Scatter in the data for fusion efficiency

The large scatter in the data at low to moderate POPG mol% represents the large variation in  $E_{FRET}$  at the level of single GUV (see figure 5B in the main text and explanation therein). Figure S10A shows FRET measurements for individual GUVs with 5 mol% POPG. This corresponds to the same dataset shown in Figure 5 in the main text for this composition. Measured  $E_{FRET}$  values range from 0.2 to 0.85 (green data in Figure S10B). One possible reason for the scatter is inhomogeneous mixing of the LUVs and GUVs (resulting in different collision frequency) and the time between mixing and imaging the individual vesicles. We also found that charged multicomponent GUVs prepared by electroformation display a large degree of membrane inhomogeneity, with a large variation in the fraction of the charged lipid in vesicles from the same batch (Lira *et al.*, manuscript in preparation) as well as variation in the composition of the POPG in the outer leaflet as a function of time after vesicle preparation (8). Presumably, these variations are the origin for the large scatter in  $E_{FRET}$  measured on different vesicles. For GUVs with high fraction of POPG, fusion is highly efficient and  $E_{FRET}$  approaches 1 (see Figure S10B), and thus the scatter is small.

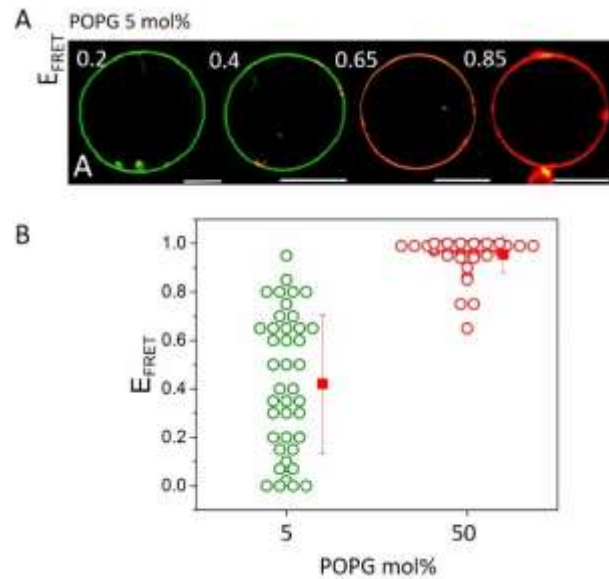


**Figure S11.** Scatter in the fusion efficiency as assessed from FRET measurements. (A) Confocal microscopy images of different GUVs in one sample prepared with 5 mol% POPG and incubated with 30  $\mu$ M fusogenic LUVs (lipid concentration). Numbers in the upper left corner indicate measured  $E_{FRET}$  values. Scale bars: 10  $\mu$ m. (B)  $E_{FRET}$  data for individual GUVs containing 5 mol% (green) or 50 mol% POPG (red). Mean average and standard deviations are also shown (red) and plotted in Figure 6 in the main text.

### S9. $E_{FRET}$ measurements in the presence of salts

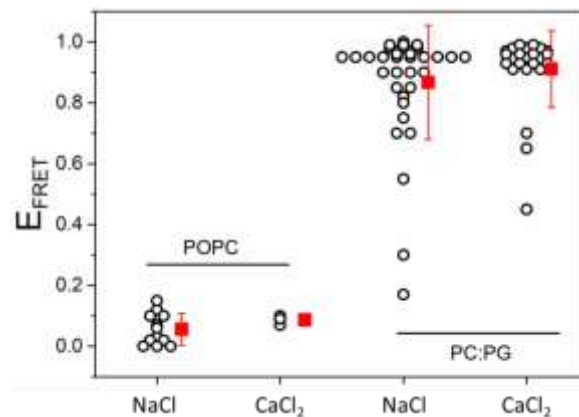


**Figure S12.** Single  $E_{FRET}$  measurements (black circles) for neutral (POPC) and negative (POPC:POPG, 1:1 mol) GUVs incubated with 30  $\mu$ M fusogenic LUVs in the presence of 100 mM NaCl and 5-50 mM CaCl<sub>2</sub>. Average values and standard deviations are also shown (red).

## S10. FRAP experiments

**S10.1 Setup and conditions.** GUVs of different compositions containing 0.5 mol% DPPE-Rh were investigated using fluorescence recovery after photobleaching (FRAP). In the case of FRAP on GUVs after fusion, non-labeled GUV were incubated for 10 minutes with DPPE-Rh-containing LUVs (1  $\mu\text{M}$  lipids, which produces the same changes in FRET signal but less morphological changes). Measurements were performed after lipid mixing upon fusion and subsequent immobilization with agarose. For pre- and post-bleaching imaging, DPPE-Rh was excited at 561 nm and fluorescence detected in at 570-620 nm using a 63X (1.2 NA water-immersion) objective at 3 % laser intensity. For photobleaching, 514 nm and 561 nm lasers were used at maximum intensities. Images were taken with 128 $\times$ 128 pixels recorded in the bidirectional scan mode at 1400 Hz. Since undesired photobleaching of DPPE-Rh during recovery is negligible with the settings used, recovery curves were not corrected for photobleaching. FRAP curves were analyzed according to the theory developed in Kang et al. (9) to correct for diffusion during photobleaching; for details, see Ref. (4). For the POPC GUVs where the number of docked LUVs is high, measurements were performed on homogeneous regions of the membrane and the recovery curves were computed exclusively for the cases in which no LUVs diffused within the region of interest during the measurement.

**S10.2 Diffusion coefficients in GUVs before and after fusion.** Lipid diffusion coefficient was measured with FRAP for neutral and negative GUVs before and after fusion. In addition, measurements were also performed on the GUV mimicking the resulting membrane after fusion; that is, with composition similar to that expected after fusion as deduced from the  $E_{FRET}$  data (main text). These experiments (Figure S12) were performed in order to (i) compare lipid diffusion after LUV-GUV fusion (red) with diffusion of lipids in similar membranes without fusion (black) and with the fused membrane mimetics (blue), and (ii) to probe the validity of the membrane compositions of fused GUVs as predicted from  $E_{FRET}$  measurements as described in Section S5.2. Figure S12 and Table S1 show diffusion coefficient for all measured systems. In agreement with previous data (4), charged GUVs display slower diffusion. Because of the small fusion efficiency with neutral membranes the diffusion coefficient is only weakly affected. In contrast, high fusion efficiency with negative GUVs results in stronger decrease in lipid diffusion. The mimetic mixtures reflect these trends well.

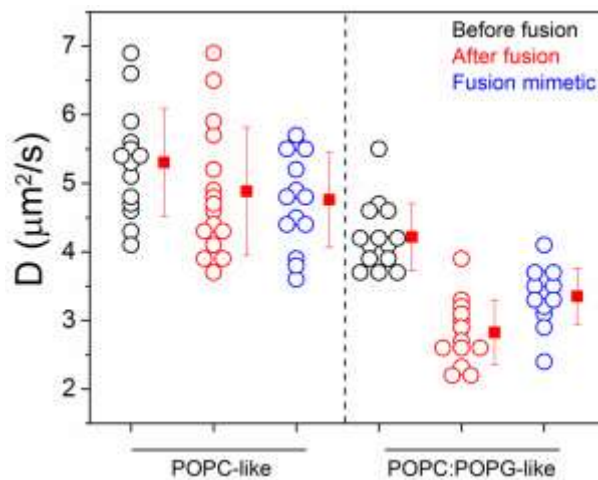


**Figure S13.** Diffusion coefficients in neutral (left) and negative (right) membranes before and after fusion. Black: initial GUV composition (containing 0.5 mol% DPPE-Rh). Red: initially non-labeled GUVs after fusion with LUVs containing 5 mol% DPPE-Rh (LUV final lipid concentration was 1  $\mu\text{M}$ ). Blue: mimic of the GUV composition (containing 0.5 mol% Rh) after fusion as deduced from FRET measurements: POPC:DOPE:DOTAP 9:0.5:0.5 (left) and POPC:POPG:DOPE:DOTAP 0.25:0.25:0.25:0.25 (right).

**Table S1.** Summary of diffusion coefficients of DPPE-Rh ( $\mu\text{m}^2/\text{s}$ ) for the different systems. Errors are standard deviations from the mean. The values correspond to figure S12.

POPC (before)	POPC (after)	POPC (mimetic)	POPC:POPG (before)	POPC:POPG (after)	POPC:POPG (mimetic)
5.3±0.8	4.9±0.9	4.7±0.7	4.2±0.5	2.8±0.5	3.3±0.4

## S11. Lipid mixing assay using FLIM-FRET

**S11.1 Data acquisition.** GUVs (30  $\mu\text{L}$ ) containing 0.5 mol% DPPE-NBD and DPPE-Rh containing LUVs (30  $\mu\text{M}$  lipid concentration) were mixed in an Eppendorf tube for 10 minutes to 130  $\mu\text{L}$  total solution in 200 mM glucose as described above. An aliquot was then transferred for observation. Fluorescence lifetime imaging microscopy (FLIM) was performed on an inverted microscope (IX83, Olympus) equipped with a time correlated single photon counting (TCSPC) card (SPC150, Becker & Hickl). Samples were illuminated via a 60x water immersion objective lens (UPLSAPO, Olympus). The NBD label was excited by a 485 nm pulsed diode laser with a 40 MHz repetition rate. Emission was collected via the same objective and filtered from the excitation light by a 550 nm dichroic and a 500 – 550 nm emission filter for NBD fluorescence. Emission from the Rh label was also collected (to directly observe LUV fusion) using a 640 nm dichroic and a 580 – 630 nm emission filter. Typical image acquisition times were approximately 30 s depending on the signal to noise ratio of the GUV under investigation.

**S11.2 Image processing and decay fitting.** In order to measure the FRET efficiency using FLIM, a region of interest was created at the membrane of the GUVs and all the pixels were binned to obtain a single fluorescence decay (NBD channel only). The decays were then fitted with a bi-exponential decay model using SPCImage (Becker & Hickl) fitting software:

$$I(t) = I_0(A_1e^{-t/\tau_1} + A_2e^{-t/\tau_2}) \quad (\text{S2})$$

where  $I(t)$  is the intensity at time  $t$ ,  $I_0$  is the intensity at  $t = 0$ , and  $A_1$  and  $A_2$  are pre-exponentials factors associated with lifetime components  $\tau_1$  and  $\tau_2$ , respectively. The amplitude-weighted mean fluorescence lifetime ( $\tau$ ) could then be calculated as

$$\tau = A_1\tau_1 + A_2\tau_2 \quad (\text{S3})$$

To measure the FRET efficiency for a particular membrane composition,  $\tau$  was obtained from GUVs both before ( $\tau_{before}$ ) and after ( $\tau_{after}$ ) incubation with the LUVs using two populations of GUVs. The FLIM-FRET efficiency is given as

$$E_{FRET}^{\tau} = 1 - \tau_{after}/\tau_{before} \quad (\text{S4})$$

**S11.3 FLIM-FRET fusion.** In order to cross validate intensity-based FRET to measure fusion efficiency, we performed fluorescence lifetime-based FRET or FLIM-FRET. Representative FLIM maps of the mean donor (NBD) fluorescence lifetime ( $\tau$ ) are shown in Figure S13A. All data were fitted well with a double-exponential decay model (Equation S2) as shown by the residuals in S13B. The amplitude weighted lifetimes were calculated for the entire membrane according to Equation S3 and compared among the different compositions before and after fusion for individual vesicles (Figure S13B). Figure S13C shows FLIM-FRET values,  $E_{FRET}^{\tau}$ , calculated from Equation S4 after fusion using mean average lifetime values across all GUVs.



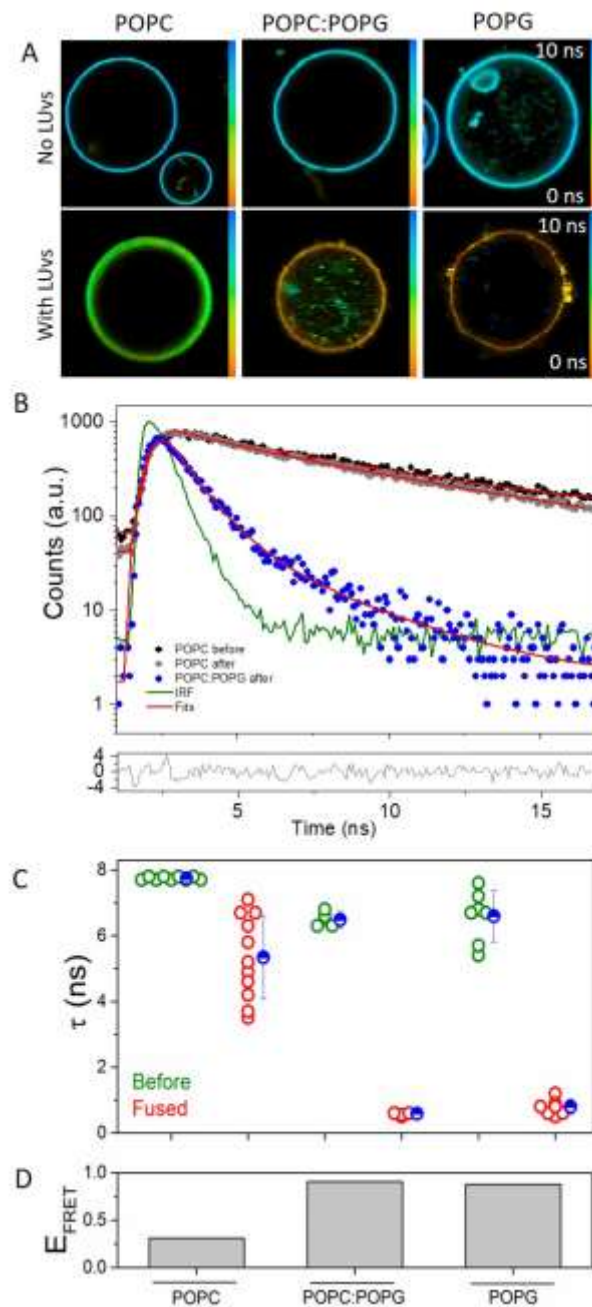


**Figure S14.** Fluorescence lifetime-based FRET measurements on GUVs. (A) FLIM maps of GUVs of different compositions before (no LUVs) and after (with LUVs) incubation with 30  $\mu\text{M}$  (lipids) LUVs. On the right, mean fluorescence lifetime ( $\tau$ ) scales in the range of 0-10 ns. (B) Exemplary fluorescence lifetime decay curves for POPC before (black) as well as POPC (grey) and POPC:POPG (blue) after fusion with LUVs. The fits to the data and the instrument response function (IRF) are given, as well as the residuals of the fits for POPC before fusion. (C) Individual lifetime values for the different conditions. Each data point represents one GUV. Mean average and standard deviations are also shown. (D) Calculated FLIM-FRET values,  $E_{FRET}^{\tau}$ , for the GUVs after fusion.

**Table S2. Measured parameters from intensity-based ( $E_{FRET}$ ) and FLIM-based ( $E_{FRET}^{\tau}$ ) FRET for GUVs of different compositions. Mean averages are given with standard deviations.**

POPG fraction, mol%	Intensity FRET, $E_{FRET}$	$\tau_{before}$	$\tau_{after}$	FLIM-FRET, $E_{FRET}^{\tau}$
0	0.38±0.30	7.74±0.05	5.34±1.27	0.31±0.07
50	0.98±0.01	6.49±0.25	0.59±0.04	0.91±0.07
100	0.95±0.01	6.59±0.78	0.80±0.22	0.88±0.27

## Movie captions

**Movie S1.** Real-time fusion of LUVs to a green POPC:POPG (1:1 mol) in a microfluidic chamber. The onset of LUV flow coincides with the change in GUV fluorescence due to FRET.

**Movie S2.** Bulk addition of fusogenic LUVs (red) to POPC:POPG (95:5 mol) GUVs (green). LUVs dock to the GUV surface increasing membrane tension, eventually resulting in vesicle rupture.

**Movie S3.** Bulk addition of fusogenic LUVs (red) to a pure POPG GUV (green). Docking is immediately followed by efficient fusion, resulting in a large change in GUV color and a significant increase in area, detected as membrane fluctuations. Upon saturation, the GUV relaxes back to its quasi-spherical shape and the acquired area is stored in membrane folds.

**Movie S4.** Fusion of fluorescent LUVs to non-fluorescent negative POPC:POPG (1:1 mol) GUVs in the presence of an AC field. The onset of (prolate) deformation coincides with the appearance of membrane fluorescence due to fusion. The area acquired from fusion is used to form buds and tubes (parallel to the AC field). At later times, the increase in spontaneous tension results in vesicle relaxation into a sphere.

## REFERENCES

1. Angelova, M. I., and D. S. Dimitrov. 1986. Liposome Electroformation. *Faraday Discuss.* 81:303-311.
2. Lira, Rafael B., R. Dimova, and Karin A. Riske. 2014. Giant Unilamellar Vesicles Formed by Hybrid Films of Agarose and Lipids Display Altered Mechanical Properties. *Biophys. J.* 107:1609-1619.
3. Weinberger, A., F. C. Tsai, G. H. Koenderink, T. F. Schmidt, R. Itri, W. Meier, T. Schmatko, A. Schroder, and C. Marques. 2013. Gel-Assisted Formation of Giant Unilamellar Vesicles. *Biophys. J.* 105:154-164.
4. Lira, R. B., J. Steinkühler, R. L. Knorr, R. Dimova, and K. A. Riske. 2016. Posing for a picture: vesicle immobilization in agarose gel. *Sci Rep* 6:25254.
5. Robinson, T., P. Kuhn, K. Eyer, and P. S. Dittrich. 2013. Microfluidic trapping of giant unilamellar vesicles to study transport through a membrane pore. *Biomicrofluidics* 7.
6. Robinson, T., P. E. Verboket, K. Eyer, and P. S. Dittrich. 2014. Controllable electrofusion of lipid vesicles: initiation and analysis of reactions within biomimetic containers. *Lab Chip* 14:2852-2859.
7. Yoon, T. Y., B. Okumus, F. Zhang, Y. K. Shin, and T. Ha. 2006. Multiple intermediates in SNARE-induced membrane fusion. *Proc. Natl. Acad. Sci. U. S. A.* 103:19731-19736.
8. Steinkühler, J., P. De Tillieux, R. L. Knorr, R. Lipowsky, and R. Dimova. 2018. Charged giant unilamellar vesicles prepared by electroformation exhibit nanotubes and transbilayer lipid asymmetry. *Scientific Reports*:in revision.
9. Kang, M., C. A. Day, A. K. Kenworthy, and E. DiBenedetto. 2012. Simplified Equation to Extract Diffusion Coefficients from Confocal FRAP Data. *Traffic* 13:1589-1600.